ANNUAL REVIEWS

*Annual Review of Astronomy and Astrophysics*

# Atomic Hydrogen in the Milky Way: A Stepping Stone in the Evolution of Galaxies

Naomi M. McClure-Griffiths,[1] Snežana Stanimirović,[2] and Daniel R. Rybarczyk[2]

[1]Research School of Astronomy and Astrophysics, Australian National University, Canberra, Australia; email: naomi.mcclure-griffiths@anu.edu.au

[2]Department of Astronomy, University of Wisconsin–Madison, Madison, Wisconsin, USA

Annu. Rev. Astron. Astrophys. 2023. 61:19–63

First published as a Review in Advance on May 30, 2023

The *Annual Review of Astronomy and Astrophysics* is online at astro.annualreviews.org

https://doi.org/10.1146/annurev-astro-052920-104851





## Keywords

atomic hydrogen, HI, interstellar medium, galaxy evolution, magnetic fields

## Abstract

Atomic hydrogen (HI) is a critical stepping stone in the gas evolution cycle of the interstellar medium (ISM) of the Milky Way. HI traces both the cold, premolecular state before star formation and the warm, diffuse ISM before and after star formation. This review describes new, sensitive HI absorption and emission surveys, which, together with high angular and spectral resolution HI emission data, have revealed the physical properties of HI, its structure, and its association with magnetic fields. We give an overview of the HI phases and discuss how HI properties depend on the environment and what its structure can tell us about feedback in the ISM. Key findings include the following:

- The mass fraction of the cold neutral medium is $\lesssim$40% on average, increasing with $A_V$ due to the increase of mean gas density.
- The cold disk extends to at least $R \sim 25$ kpc.
- Approximately 40% of the HI is warm, with structural characteristics that derive from feedback events.
- Cold HI is highly filamentary, whereas warm HI is more smoothly distributed.

We summarize future observational and simulation opportunities that can be used to unravel the 3D structure of the atomic ISM and the effects of heating and cooling on HI properties.

## Contents



## 1. INTRODUCTION

Neutral atomic hydrogen (HI) gas is the fundamental building block of galaxies. In the local Universe, fully three-quarters of the neutral gas of galaxies is in the atomic phase (Carilli & Walter 2013). HI defines a galaxy's morphology on the evolutionary path between the ionized intergalactic medium and the molecular clouds where stars are formed. HI is observed to have structure on all spatial scales, from tiny, astronomical-unit scales observed in the Milky Way (reviewed in Stanimirović & Zweibel 2018) to Galactic-scale coherent structures (e.g., McClure-Griffiths et al. 2004). And unlike many standard tracers of the structure of a galaxy, HI is not biased toward tracing star formation—it follows spiral arms with and without stars, probes gaseous disks extending beyond the stellar disk (Saintonge & Catinella 2022), and even traces the interaction between a galaxy and its starless circumgalactic environment (Cortese et al. 2021).

Around galaxies, HI exists in the form of highly diffuse, infalling gas that replenishes the disk HI reservoir and provides an important energy contribution. Cosmological simulations predict diffuse, infalling HI with column density below $10^{18}$ cm$^{-2}$ and large concentrations originating from galaxy interactions (Stevens et al. 2019). Around the Milky Way, large concentrations of

HI are associated with the Magellanic System, and smaller, dense concentrations are scattered throughout the halo and disk–halo interface as high- and intermediate-velocity clouds. The Milky Way's circumgalactic medium has been well reviewed by D'Onghia & Fox (2016) and Putman et al. (2012). Instead, we focus on the properties of HI in the disk of the Milky Way, where it is perpetually in the act of flowing between its dense, cold state and its warm, diffuse state. HI is present over a range of temperatures between ~20 K and ~8,000 K (Heiles & Troland 2003b), tracing most of the semiquiescent conditions of a galaxy. While the star formation rate of a galaxy is tightly linked to its molecular hydrogen ($H_2$) content, the star formation rate per unit HI mass varies widely among and within galaxies (Leroy et al. 2008). The standard interpretation is that star formation in galaxies is separated into two processes: one in which molecular clouds are assembled from HI and another in which stars form from $H_2$ (Schruba et al. 2011). In fact, the key regulator of star formation appears to be not the formation of $H_2$ itself but rather the formation of gas that is sufficiently shielded to reach very low temperatures so that thermal pressure cannot prevent collapse (Krumholz et al. 2011, Glover & Clark 2012). HI can therefore be considered the fuel for star formation and the key ingredient responsible for the shielding and survival of molecular gas. The transition from warm, unshielded to cold, UV-shielded HI might act as a throttle in the process of converting the interstellar medium (ISM) into stars, making it essential to the evolution of galaxies.

**Cold neutral medium (CNM):** $T_s$ = 25–250 K, 28–40% of the observed HI mass

**Warm neutral medium (WNM):** $T_s$ = 4,000–8,000 K, ~32–64% of the observed HI mass

In this review, we expand on the role of HI in a galaxy using the Milky Way as the template. We focus on the properties of the cold neutral medium (CNM) to highlight the first step in the gas evolution cycle from diffuse and warm to cold and molecular. Over the last 40 years, HI has been studied primarily in emission, and the focus has been on the large-scale structure and morphology of the warm neutral medium (WNM). Recent improvements in observational techniques for HI absorption, together with improved spatial and spectral resolution revealing cold, small-scale filamentary and fibrous structures in emission, have redirected Galactic HI studies toward the CNM as a stepping stone toward molecular cloud and star formation. Whereas the WNM is smooth and ubiquitous, the CNM has abundant small-scale structure and is better observed on small scales that are easily accessed in the Milky Way. Only in the Milky Way can we observe HI with sufficient resolution to probe the physical scales that are relevant to the cooling, condensing, and turbulent dissipation that affect how HI converts to $H_2$, as well as the feedback scales on which HI is heated and turbulence driven. Understanding the CNM as a phase of HI is essential for understanding HI as a path to molecular clouds and star formation.

The topic of HI in the Milky Way disk is vast and has been reviewed periodically (e.g., Kulkarni & Heiles 1987, Burton 1988, Dickey & Lockman 1990, Kalberla & Kerp 2009). We strive to use this review to emphasize the importance of HI in understanding how galaxies evolve and what HI can and cannot tell us about the ISM. We describe what has been revealed about the fundamental properties of HI over the last decade, what we still do not know, and finally the prospects for the field over the coming decade.

While most of us learn about the hyperfine transition of HI at 1,420.405752 MHz in our undergraduate physics classes, few learn about how it is measured and the radiative transfer that leads to its widespread usage as a tracer of mass and dynamics within galaxies. We start by revisiting some of the radiative transfer that is needed to understand how physical properties are derived from observations of HI in emission and absorption. We envision that this article can simultaneously serve as an overview for the new researcher of atomic gas in the Milky Way and external galaxies, demonstrate the constant evolution of the field, and convey the excitement of what new telescopes and simulations will reveal about the Milky Way's HI in the coming decade. For extragalactic researchers, this article should complement the review of the cold ISM of galaxies in the local Universe by Saintonge & Catinella (2022).

## 2. FUNDAMENTALS

HI, as traced by the hyperfine transition at 21 cm, is usually described by its spin or excitation temperature, $T_s$, which is related to the number density of two states of the hyperfine splitting, $n_1$ and $n_2$, of the ground state of hydrogen, by the Boltzmann equation

$$\frac{n_2}{n_1} = \frac{g_2}{g_1} e^{-h\nu/kT_s}, \quad 1.$$

where $g_2 = 3$ and $g_1 = 1$ are the statistical weights for the HI line. The spin temperature is not necessarily the same as the kinetic temperature, $T_k$, of the gas. Instead, $T_s$ is determined by the Lyman-$\alpha$ (Ly-$\alpha$) photon field, the pervasive radiation field around the rest wavelength of the hyperfine transition [such as the cosmic microwave background (CMB)], and the kinetic temperature and density, which set the collisional excitation rate (Field 1958, Liszt 2001). Connecting $T_s$ and $T_k$ requires a detailed understanding of all excitation processes for the 21 cm line. In the high-density CNM, the 21 cm transition is thermalized by collisions with electrons, ions, and other HI atoms, which drive $T_s$ toward $T_k$. In general, observers assume that $T_s \approx T_k$ for most observations of temperatures up to ~1,000 K.

At the low densities typical for the WNM, collisions cannot thermalize the 21 cm transition; therefore, $T_s < T_k$ (Field 1958, Wouthuysen 1952, Deguchi & Watson 1985, Kulkarni & Heiles 1988, Liszt 2001). The Ly-$\alpha$ radiation field can help thermalize the transition, but a very large optical depth and many scatterings of Ly-$\alpha$ photons are required to bring the radiation field and the gas into local thermal equilibrium. While the underlying atomic physics of the thermalization process is understood (Wouthuysen 1952, Field 1958, Pritchard & Loeb 2012), the details of Ly-$\alpha$ radiative transfer are complicated and depend on the topology and strength of the Ly-$\alpha$ radiation field, which are complex and poorly constrained in the multiphase ISM. It is still customary to assume a constant Ly-$\alpha$ radiation field, with a density of $10^{-6}$ Ly-$\alpha$ photons cm$^{-3}$ (Liszt 2001), in theoretical and numerical calculations.

### 2.1. Overview of Phases

The balance of heating and cooling processes in the ISM results in a medium with a range of temperatures and densities. Over a narrow range of pressures, HI can be approximated as a two-phase medium (Field et al. 1969, Wolfire et al. 1995, Cox 2005) in which the warm and cold phases coexist in pressure equilibrium. Of course, the ISM is not entirely atomic; McKee & Ostriker (1977) proposed the three-phase model in which CNM clouds are surrounded by the WNM and those neutral clouds are embedded within a supernova-heated hot, ionized medium (Cox & Smith 1974)—all in pressure equilibrium set by the supernovae. Subsequent refinements to the theoretical models noting, for example, the effects of turbulent pressure have led to a much more complex structure of phases in the ISM and the understanding that the CNM plus WNM can occupy as much volume as the hot, ionized medium (e.g., Wolfire et al. 2003, Audit & Hennebelle 2005, Hill et al. 2018, Bialy & Sternberg 2019).

The thermal equilibrium range of pressures where both WNM and CNM can exist is set by the balance of heating, $\Gamma$, and cooling, $\Lambda$, leading to the well-known phase diagram showing thermal pressure as a function of density [$P = T \times \Gamma/\Lambda(T)$]. As shown in **Figure 1*a***, for solar metallicity, the range of stable pressures where both WNM and CNM can exist is $1{,}500 < P_k < 10^4$ cm$^{-3}$ K, with the upper limit typically closer to ~3,000 cm$^{-3}$ K (Field et al. 1969, Wolfire et al. 2003). Along the curve where $dP/dn > 0$, gas is thermally stable, meaning that if a gas parcel is perturbed from the equilibrium, it will either cool or heat to return to the same equilibrium position. These positions define the WNM at the low-density end and the CNM at the high-density end. There is another equilibrium point on the phase diagram where $dP/dn < 0$ that corresponds to the

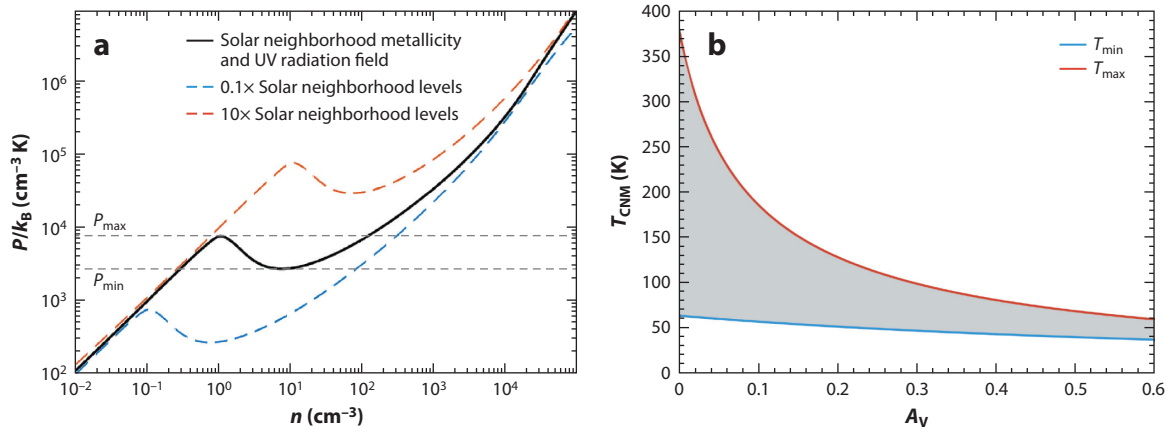


**Figure 1**

(*a*) Phase diagram for heating and cooling balance in the interstellar medium. The solid black line represents the Solar Neighborhood metallicity and UV radiation field. The dashed curves represent UV radiation fields that are respectively 0.1 and 10 times the Solar Neighborhood levels. For multiphase HI to exist, the thermal pressure is required to be within a well-defined range, $P_{min}$ to $P_{max}$, denoted by the dashed gray lines. (*b*) The expected cold neutral matter (CNM) kinetic temperature based on the heating–cooling equilibrium as a function of visual extinction ($A_V$) (Bialy & Sternberg 2019, Bialy 2020). At higher optical extinction, HI is shielded from external radiation by dust, which results in a lower radiation field and reduces the range of CNM temperatures allowed. Panel *a* adapted with permission from Bialy & Sternberg (2019). Panel *b* provided by S. Bialy.

intermediate temperature and density regime. This region is thermally unstable, meaning that if an HI parcel is perturbed out of equilibrium it will either cool or heat such that it moves to one of the two stable solutions. This regime defines the unstable neutral medium (UNM). Based on theoretical and numerical studies, the UNM temperature is expected to be in the range ~250–4,000 K, although it depends on the details of the local heating and cooling (Field et al. 1969; Wolfire et al. 1995, 2003).

The dominant heating mechanism for diffuse ISM is the photoelectric effect on dust grains. While the heating rate per unit volume depends on the starlight intensity and is a function of grain properties, including charging (which depends on the gas ionization), it does not depend strongly on temperature. As discussed by Bialy & Sternberg (2019), at very high densities or very low metallicities, $H_2$ heating and cooling become important. On the other side of the balance equation, the key cooling mechanism for cool HI (10–$10^4$ K) is the [CII] 158 μm fine-structure line emission, followed by the [OI] 63 μm fine-structure line emission. As these transitions are excited by collisions with hydrogen atoms and electrons, the cooling rate depends on the fractional ionization. At warmer temperatures ($\gtrsim 10^4$ K), Ly-α emission is the dominant coolant. As these are collisional processes, the cooling rate per volume depends strongly on temperature, $\Lambda(T)$.

The details of the classical steady-state heating and cooling processes and the resulting HI phases were revised in recent modern treatments by Wolfire et al. (2003) and Bialy & Sternberg (2019). Bialy & Sternberg (2019) explored a broad parameter space of metallicity, the interstellar radiation field, and the cosmic-ray ionization rate and showed how these affect the thermal structure of HI. As local conditions of the ISM change, so do the HI phases. For example, at low metallicity (0.1 solar) and in the case of dust and metal abundance being reduced by the same amount, the photoelectric heating is less effective, resulting in the expectation that the CNM should be colder. As shown in **Figure 1*a***, when the UV radiation field increases by a factor of 10, the equilibrium curve shifts to the right, and the CNM and WNM coexist at a higher pressure.

**Unstable neutral medium (UNM):** $T_s$ = ~250–4,000 K, ~20–28% of the observed HI mass

Other local conditions, such as column density, can also modify the HI thermal structure. **Figure 1*b*** shows how varying the column density or optical extinction $A_V$ has a strong effect on the range of predicted CNM temperatures, $T_{min}$ to $T_{max}$. At low $A_V$, the CNM temperature has a broad distribution (~70–350 K), while at $A_V > 0.2$, the CNM temperature range becomes very narrow, settling around 50 K for $A_V \sim 1$. This is due to dust shielding effectively reducing the ambient radiation field.

Most of the detailed analytical prescriptions for heating and cooling processes consider steady-state thermal equilibrium (e.g., McKee & Ostriker 1977, Wolfire et al. 2003, Bialy & Sternberg 2019). However, supernovae, stellar winds, and many other dynamical processes constantly disrupt the heating–cooling balance and broaden the pressure distribution function. Furthermore, turbulent processes constantly drive gas into the unstable gas regime. To observe how various dynamical sources set the CNM, UNM, and WNM distributions, we require numerical simulations.

## 2.2. Observable Quantities

The HI line is observed in either emission or absorption, depending on the optical depth, $\tau(v)$ and, by extension, the temperature of the gas, $T_s$. Based on the physics of spectral line profiles (and assuming a Gaussian line profile), the peak optical depth of the HI line is related to the gas spin temperature; the full width at half-maximum (FWHM) linewidth, $\delta v$; and the column density, $N_{HI}$, as

$$\tau_0 = \frac{N_{HI}\ (\mathrm{cm^{-2}})}{1.94 \times 10^{18}\ (\mathrm{cm^{-2}\ K^{-1}\ km^{-1}\ s})} \frac{1}{T_s\ (\mathrm{K})\, \delta v\ (\mathrm{km\ s^{-1}})}. \quad 2.$$

For a given column density of HI, $\tau_0$ is inversely proportional to $T_s$. In fact, because $\delta v$ for a Boltzmann thermal distribution goes as $\delta v = 0.213\sqrt{T_k}$ km s$^{-1}$, when $T_s \approx T_k$ then $\tau_0 \propto T_s^{-3/2}$. If we assume a WNM temperature of $T_s \sim 8{,}000$ K, which has a thermal velocity linewidth of $\delta v \sim 19$ km s$^{-1}$, we can easily see that for any column density observed in the Milky Way ($N_{HI} < 10^{22}$ cm$^{-2}$) the WNM is optically thin ($\tau_0 < 10^{-2}$) and would require sensitive observations to be detected in absorption.

A primary observational property of HI in emission is the brightness temperature, $T_b(v)$, which is measured as a function of Doppler velocity and related to the optical depth, $\tau(v)$, and the spin temperature, $T_s$, as

$$T_b(v) = T_s(1 - e^{-\tau(v)}). \quad 3.$$

Again considering WNM temperatures of 8,000 K, and if $\tau \ll 1$, the brightness temperatures are approximated as $T_b \approx T_s\tau$ and can range from very small to ~100 K. Similar arguments about temperature and density show that HI with nonnegligible optical depths, observed via absorption, is mostly CNM.

It can be tempting to assume that HI absorption mostly traces CNM and that HI emission traces WNM, but the definition of phases in emission is not nearly so clear. If $T_s \sim 50$ K, then optical depths of $\tau \approx 0.5$ still produce HI brightness temperatures that are significantly larger than the Kelvin or sub-Kelvin observational limits. Conversely, observations with very high optical depth sensitivity can detect the warm (or at least the unstable) neutral medium in absorption (Roy et al. 2013a, Murray et al. 2018). The separation between the WNM and CNM in both emission and absorption therefore relies on high-sensitivity observations and high spectral resolution for resolving narrow linewidths.

To calculate the column density of a single homogeneous HI feature, we need its excitation temperature and the optical depth:

$$N_{\rm HI} = CT_{\rm s} \int \tau(v)\,{\rm d}v, \qquad 4.$$

where $C = 1.823 \times 10^{18}$ [cm$^{-2}$ (km s$^{-1}$ K)$^{-1}$]. If there are several HI features along the line of sight, the column density for each feature must be treated individually with its own $T_{\rm s}$ (e.g., Heiles & Troland 2003a). In the absence of full information about the distribution of spin temperatures with respect to velocity, it is often necessary and prudent to assume that the gas is isothermal, such that only one temperature is represented at each velocity channel, where

$$T_{\rm s}(v) \approx \frac{T_{\rm b}(v)}{1 - e^{-\tau(v)}}. \qquad 5.$$

The column density of the entire line of sight can then be written as

$$N_{\rm HI,iso} = C \int \frac{\tau(v) T_{\rm b}(v)}{(1 - e^{-\tau(v)})} {\rm d}v, \qquad 6.$$

as proposed by Dickey & Benson (1982) and developed by Chengalur et al. (2013). Clearly, for small optical depths, Equation 6 reduces to the well-known simplification

$$N_{\rm HI,thin} = C \int T_{\rm b}(v) {\rm d}v. \qquad 7.$$

As described above, HI in emission can trace both the CNM and the WNM. HI emission on its own provides an estimate of total column density if we assume optically thin emission ($\tau \ll 1$; Equation 7) and an upper limit on the kinetic temperature of the gas, $T_{\rm k}$, through its FWHM linewidth, $\delta v$:

$$T_{\rm k}\,(K) \leq 22\,[\delta v\,({\rm km\ s^{-1}})]^2. \qquad 8.$$

CNM temperatures of ~20–200 K produce thermal linewidths of only 1–2 km s$^{-1}$, while WNM temperatures of ~3,000–8,000 K produce thermal linewidths of 11–20 km s$^{-1}$.

HI observers directly measure optical depth, $\tau(v)$, plus the linewidth, $\delta v$, of individual features in the absorption spectrum, and the corresponding brightness temperature, $T_{\rm b}(v)$, through emission. However, HI emission and absorption can be combined to solve for the spin temperature, $T_{\rm s}$, of an HI feature, as described in Equation 3. From here, contributions from turbulent motions of the gas to the linewidth $\delta v$ can be estimated (Heiles & Troland 2003b).

## 3. NUMERICAL SIMULATIONS OF HI

Numerical simulations of the ISM are invaluable for understanding how the many, varied physical processes of the ISM shape HI over a wide range of environments. Huge advances in computational facilities and techniques in recent years have moved from 2D idealized boxes with basic feedback processes driven artificially at a fixed rate (Audit & Hennebelle 2005) to 3D, self-consistent, parsec-scale, multiphase simulations that track the effects of different feedback sources, such as supernovae, stellar winds, cosmic rays, and radiation (Kim et al. 2013, Kim & Ostriker 2017, Rathjen et al. 2021). Even still, numerical simulations are not able to provide the dynamic range needed to self-consistently track the HI from large-scale, infalling, diffuse gas all the way to molecular clouds within a larger galactic context (outflows, disk–halo interface regions, galactic rotation). However, many simulations have demonstrated the importance of including the large-scale fundamental processes to shape HI in realistic ways. Hopkins et al. (2012, 2018, 2020) showed that stellar feedback is essential to reproduce realistic HI morphology observed in the Milky Way

and other galaxies; without it, simulated gas density distributions are too high and lead to runaway star formation and unrealistic phase distributions. Similarly, the distribution of spatial power, represented by the spatial power spectrum (SPS), requires stellar feedback to match observations (Iffrig & Hennebelle 2017, Grisdale et al. 2018).

Over the last two decades, many simulations have focused on high-resolution models of the highly dynamic and turbulent character of the ISM in an attempt to reproduce the observed thermal and morphological structure of HI. For example, Audit & Hennebelle (2005) showed that a collision of incoming turbulent flows can initiate fast condensation from WNM to CNM. Koyama & Inutsuka (2002) and Mac Low et al. (2005) explored how shocks driven into warm, magnetized, and turbulent gas by supernova explosions create dense, cold clouds. The latter study showed a continuum of gas temperatures, with the fraction of the thermally unstable HI constrained by the star formation rate. Ntormousi et al. (2011) modeled the formation of cold clouds in a realistic environment of colliding superbubbles and showed that cold, dense, and filamentary structures form naturally in the collision zone. As HI is the seed for the formation of $H_2$, many simulations start with initial conditions for the diffuse HI and follow development of the CNM first, and then $H_2$ (Glover et al. 2010, Vázquez-Semadeni et al. 2010, Clark et al. 2012, Valdivia et al. 2016, Seifried et al. 2022). Simulations (e.g., Vázquez-Semadeni et al. 2010, Goldbaum et al. 2011) have suggested that the CNM plays a central role in the formation and evolution of molecular clouds via accretion flows. However, exactly how the HI cycles through various phases in the process of building molecular clouds is still not clear. Numerical simulations by Dobbs et al. (2012) suggested that it is the UNM that is direct fuel for molecular clouds.

A key power of numerical simulations is in providing data for a direct comparison with observations. We summarize two topics where such comparisons are important: the HI mass fraction and synthetic line profiles.

### 3.1. HI Mass Fraction as a Function of Phase

The mass fraction of different HI phases is a useful quantity to predict because it can be constrained observationally, which helps clarify the important processes. The existence of bimodal HI distributions has become a stable feature in recent simulations. While the inclusion of different feedback sources (supernovae, stellar winds, UV radiation from HII regions) initially resulted in a broad density distribution without two well-separated HI phases (e.g., Mac Low et al. 2005), more recent magnetohydrodynamic simulations have easily produced the bistable HI structure with the CNM and WNM as distinct density peaks (Kim et al. 2014, Kim & Ostriker 2017, Hill et al. 2018). Two suites of simulations with the highest resolution that focus on the thermal state of HI are TIGRESS (Kim & Ostriker 2017) and SILCC (Walch et al. 2015, Rathjen et al. 2021). The TIGRESS simulations show that although turbulence, temporal fluctuations of the heating rate, and expanding superbubbles continuously populate the UNM phase, thermal instability and rapid cooling reduce the amount of UNM and result in most of the HI following thermal equilibrium and being in the two-phase state (**Figure 2**). Even when varying the heating rate significantly, Hill et al. (2018) showed that the two-phase HI persisted and that the mass fraction of the thermally unstable HI was below 20%.

While recent simulations agree about the existence of bistable HI, significant differences exist in the mass fraction across different phases. **Figure 2** shows predictions for the HI fraction of total column density at a given $T_s$ from several simulations. SILCC predicts a significantly higher CNM mass fraction (∼50%) relative to TIGRESS (<20%). The UNM fractions seem to agree at ∼20–30%. Surprisingly, different feedback channels do not have a large effect on the HI phase fractions in TIGRESS (C.-G. Kim, personal communication), while slightly larger differences are observed in SILCC (Rathjen et al. 2021).

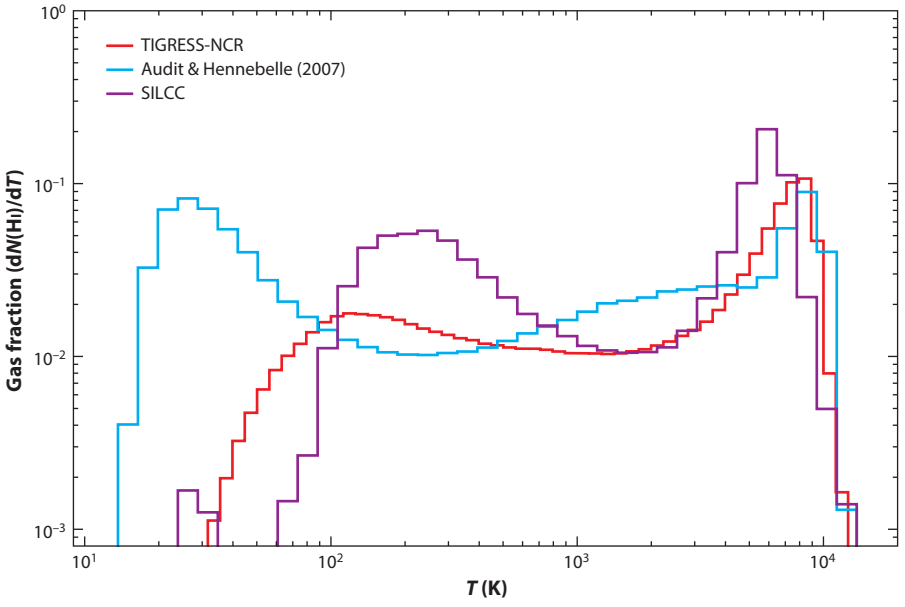


**Figure 2**

Fraction of total column density at a given spin temperature, as predicted from the 3D simulations TIGRESS-NCR (Kim et al. 2022) and SILCC (Rathjen et al. 2021) and from the 2D simulation by Audit & Hennebelle (2005). Data were kindly provided to the authors by C.-G. Kim, T.E. Rathjen, and P. Hennebelle.

## 3.2. Synthetic HI Line Profiles

Synthetic HI spectra in emission and absorption are essential for comparing observations with simulations. Through direct comparison, it is possible to test the reliability of simulations and investigate biases in observational processing techniques (Haworth et al. 2018). As an example, using TIGRESS, Kim et al. (2014) provided thousands of synthetic spectra that Murray et al. (2018) analyzed exactly as observed HI spectra. By comparing the identified spectral features in the synthetic spectra with 3D density structures, Murray et al. (2018) estimated the completeness and accuracy of the radiative transfer approach used to observationally estimate $T_s$. Similarly, considering correspondence between the true positions and observed radial velocities of molecular clouds, Beaumont et al. (2013) showed that the superposition of clouds along the line of sight introduces significant uncertainty to observational estimates of cloud mass, size, and velocity dispersion. While this study focused specifically on carbon monoxide (CO) and denser environments, masses and sizes of HI structures are similarly affected by line-of-sight complexities. Simulated spectra will become even more important in the future to assess the accuracy of automated data handling routines that will be used by large surveys.

The comparison of simulated and observed spectra is important to fully constrain the excitation processes for the WNM. A large uncertainty exists in the excitation temperature of HI ($T_s$), especially for the WNM, where the collisional excitation is insignificant. Excitation by Ly-α resonant scattering can be a dominant excitation mechanism (Liszt 2001, Kim et al. 2014). Direct Ly-α radiation transfer in a realistic ISM has recently revealed that the Ly-α excitation in the solar vicinity is efficient enough to make $T_s$ as high as the gas kinetic temperature, $T_k \sim 7{,}000$–$8{,}000$ K (Seon & Kim 2020), in agreement with the observational result obtained by Murray et al. (2014).

## 4. OBSERVATIONS OF HI

Observations of HI have overwhelmingly focused on HI emission, which is used to study the structure of HI, measure column density with assumptions about optical depth, and measure velocity linewidths. Recently, HI absorption surveys have increased in both coverage and sensitivity. However, absorption observations target a limited set of directions but provide measurements of optical depth as well as linewidth. The power of HI is truly unlocked when absorption and emission are brought together.

### 4.1. HI in Emission

Based on the relations described in Section 2.2, the brightness temperature of HI emission is proportional to column density, making HI emission a powerful tracer of the distribution of HI. Furthermore, modern observational surveys can measure HI emission at all spatial positions, producing a fully sampled atlas of the distribution of HI. Historically, this emission has been used to describe the 3D distribution of the Milky Way (Section 6.4), as well as the overall morphology of the atomic ISM (Section 6). The spatial structure of HI emission was recently extended to trace the disk–halo interaction (Section 6) and to show its connection with magnetic fields (Section 6.2). Relying on its complete sampling of all spatial scales, statistical studies of HI emission have been used to elucidate the turbulent properties of the medium (Section 6.3).

For many years, HI observers have been working to decompose the WNM and CNM components of the emission on the basis of velocity dispersion (e.g., Kulkarni & Fich 1985, Verschuur 1995). The decomposition is challenging because the WNM is bright, is spatially pervasive, and has broad linewidths, whereas the CNM has narrow linewidths and is weak unless $\tau \approx 1$, meaning that its contribution to $T_b(v)$ is easily swamped by the WNM. Sophisticated techniques for semi-autonomous decomposition have recently been used on large-area HI emission surveys to derive estimates of the gas-phase fractions of the CNM, UNM, and WNM and to consider differences in the structure of the WNM and CNM (Haud & Kalberla 2007, Kalberla & Haud 2018, Marchal et al. 2019). For example, Kalberla & Haud (2018) used Gaussian decomposition on the HI4PI survey (Ben Bekhti et al. 2016) to show that the CNM is largely filamentary. Marchal & Miville-Deschênes (2021) used a different decomposition technique, called ROHSA (Marchal et al. 2019), that employs spatial continuity between adjacent spectra to derive a regularized Gaussian fit over a high-latitude HI field. Murray et al. (2020) took a different approach and used machine learning with a convolutional neutral network, informed by HI absorption spectra, to separate the CNM from the WNM in emission. These various techniques provide estimates of the CNM fraction and show structural differences between the phases.

**4.1.1. Summary of 21 cm emission surveys.** HI surveys of emission in the Milky Way have traditionally been carried out with single-dish radio telescopes. With each decade since the discovery of the HI line by Ewen & Purcell (1951), the angular resolution and sky coverage of HI surveys have increased by roughly a factor of two. The last century ended with the famous Leiden–Argentine–Bonn (LAB) compilation (Kalberla et al. 2005), which provided a uniform survey at 30 arcmin angular resolution, 1 km $s^{-1}$ velocity resolution, and ~100 mK brightness sensitivity over the whole sky. As reviewed by Kalberla & Kerp (2009), the LAB survey formed the basis for much of what we know about the large-scale HI structure of the Milky Way.

At the end of the twentieth century, two technical advances, multibeam receivers and interferometric mosaicing, came to radio telescopes and pushed HI surveys into a new era. The first of these, the multibeam receiver, decreased the survey time required to reach high sensitivity over extensive sky areas with large (60–300 m) telescopes. The multibeam receivers on the Parkes

telescope (13 beams), the Effelsberg telescope (7 beams), and the Arecibo radio telescope (7 beams) all produced a new generation of surveys covering large areas at resolutions less than 16 arcmin. The Parkes Galactic All-Sky Survey (McClure-Griffiths et al. 2009, Kalberla et al. 2010, Kalberla & Haud 2015) and the Effelsberg–Bonn HI survey (Winkel et al. 2010) were combined to produce HI4PI (Ben Bekhti et al. 2016) at 16 arcmin. The all-sky composite HI4PI shows structures to be traced across the whole sky and enables statistically complete studies of phase distributions to be conducted in different regions with the same data. The most recent and highest-resolution single-dish survey is GALFA-HI, conducted with Arecibo (Peek et al. 2018). GALFA-HI has pushed single-dish HI emission surveys into a new realm of sensitivity coupled with angular and spectral resolution. Unlike many previous surveys of HI emission, GALFA-HI has a velocity resolution of $\sim$0.2 km s$^{-1}$, revealing very fine velocity gradients across the HI emission sky.

Interferometric mosaicing came into common practice at the same time as multibeam receivers. By combining observations of many overlapping fields of view, interferometric mosaicing enables observations of a large area of sky and the recovery of larger angular scales than accessible through a single pointing. Mosaicing was originally proposed by Ekers & Rots (1979) but was not widely adopted for diffuse imaging until the 1990s, when Sault (1994) perfected the technique for the Australia Telescope Compact Array (ATCA) starting with the Small Magellanic Cloud (Staveley-Smith et al. 1997). The next development, combining interferometric mosaics with image cubes from single-dish telescopes (Stanimirović et al. 1999, Stanimirović 2002), resulted in HI cubes that recovered emission on all angular scales from many degrees to the resolution limit of the array, typically 1–3 arcmin. This technique was adopted by the Dominion Radio Astrophysical Observatory's Synthesis Telescope with the Canadian Galactic Plane Survey (CGPS; Taylor et al. 2003) and the DRAO HI Intermediate Galactic Latitude Survey (Blagrave et al. 2017), the ATCA Southern Galactic Plane Survey (SGPS; McClure-Griffiths et al. 2005), and, finally, the Very Large Array (VLA) Galactic Plane Survey (VGPS; Stil et al. 2006).

The time required to reach a given brightness sensitivity goes as the inverse square of the longest baseline of the interferometer, forcing a constant trade-off between resolution and brightness sensitivity. Because the time needed to survey large areas at high resolution and with high surface brightness sensitivity with interferometers is prohibitive, the high angular resolution interferometric surveys were limited to much smaller aerial regions than single-dish surveys, focusing primarily on the Galactic Plane and a single intermediate-latitude patch. Recently, the VLA conducted a new Galactic Plane survey, THOR (Beuther et al. 2016, Wang et al. 2020b), with the goal of improving the angular resolution of the VGPS to 20 arcsec. Together, the HI surveys of the last 20 years have demonstrated the inherent wealth of structure in the Galactic HI over all size scales, which we discuss in Section 6, below.

### 4.2. HI Continuum Absorption

The most powerful way to constrain the CNM, with its moderately high optical depths, is via absorption against continuum background sources. To see how the CNM can be constrained, let us extend the radiative transfer discussion from Section 2.2. In general, the simple radiative transfer equation for a single HI feature given in Equation 3 will include a contribution of the diffuse radio continuum emission, expressed as brightness temperature of the sky, $T_{\rm c,sky}$, that incorporates the CMB and the Galactic synchrotron emission, varying with position. Absorption measurements can be made on radio source (usually a quasar or a radio galaxy) with a continuum spectrum, $T_{\rm c,bg}$. The radiative transfer equation in the direction of the background source then becomes

$$T_{\rm b}(v) = T_{\rm s}(1 - e^{-\tau(v)}) + (T_{\rm c,sky} + T_{\rm c,bg})e^{-\tau(v)}. \quad 9.$$

Comparing HI spectra obtained in the direction of the background source and spectra close to the background source (i.e., off-source, where $T_{c,bg} = 0$ K), under the assumption of uniform foreground HI emission and $T_s$, we can solve Equation 9 for both $T_s$ and $\tau(v)$. Equation 4 then provides an estimate of the column density, $N_{HI}$, of HI structures along the line of sight.

For the uniform HI emission assumption to work, high angular resolution is required so that the off-source spectrum samples a line of sight very similar to that of the on-source spectrum. In this respect, interferometers are highly advantageous, and they resolve out the large-scale structure to help simplify Equation 9 with $T_{c,sky} \approx 0$ K. Because interferometric mapping with the inclusion of all spatial scales is time consuming, single-dish telescopes are often used for off-source measurements of $T_b(v)$. However, because the emission fluctuations within the single-dish beam can contaminate absorption measurements, more complex strategies for estimating spatial variations of HI emission are required (e.g., Heiles & Troland 2003a). A complicating factor when using single-dish telescopes to provide off-source spectra is the mismatch of beam sizes of emission and absorption spectra when solving the radiative transfer equations for $T_s$ and $\tau(v)$. The HI absorption spectrum samples a very small solid angle occupied by the background (often point) source, while the HI emission is typically measured on arcminute scales (Section 4.1). This can result in the absorption features not having clear corresponding emission components.

The biggest complication in deriving both $T_s$ and $\tau(v)$ is that both $T_b(v)$ and $\tau(v)$ spectra usually contain multiple velocity components, resulting in a need for more sophisticated radiative transfer calculations. Several approaches have been used to address this issue, such as fitting individual components with Gaussian functions (e.g., Heiles & Troland 2003a), using the slope method (e.g., Mebold et al. 1997, Dickey et al. 2003), or simply working with integrated spectral quantities (e.g., Equations 5 and 6). This problem is exacerbated at low Galactic latitudes, where lines of sight have many velocity components. A related concern is whether selected velocity structures correspond to real physical structures in the ISM or are possibly seen as superpositions of many unresolved structures. Such superpositions introduce biases in observational estimates of $T_s$ and $\tau(v)$ and have been investigated by numerical simulations (e.g., Hennebelle & Audit 2007, Kim et al. 2014). Murray et al. (2017) used synthetic spectra from Kim et al. (2014) to show that the completeness of recovering $T_s$ with Gaussian fits depends strongly on the complexity of the HI spectra. For simulated high-latitude lines of sight ($|b| > 50$ deg), 99% of identified structures in radial velocity had corresponding density features. However, the recovery completeness dropped to 67% for 20 deg $< |b| <$ 50 deg and 53% for 0 deg $< |b| <$ 20 deg. As line-of-sight complexity increases, completeness decreases, reflecting the difficulty in unambiguously associating spectral features in emission and absorption in the presence of line blending and turbulence.

**4.2.1. Summary of 21 cm continuum absorption surveys.** Due to the high optical depth of the CNM, 21 cm absorption signatures have been easy to detect, even with low-sensitivity observations (e.g., Hughes et al. 1971; Radhakrishnan & Goss 1972; Knapp & Verschuur 1972; Lazareff 1975; Dickey et al. 1977, 1978; Crovisier et al. 1978; Payne et al. 1978; Dickey & Benson 1982; Belfort & Crovisier 1984; Braun & Walterbos 1992; Heiles & Troland 2003a). Perhaps the most influential single-dish absorption survey was the Millennium Arecibo 21 Centimeter Absorption-Line Survey, composed of 79 HI absorption and emission spectral pairs spread over the full Arecibo Observatory sky (Heiles & Troland 2003a).

The optical depth of the UNM and WNM is very low ($\tau \leq 10^{-2.5}$), and highly sensitive observations are required to detect these phases in absorption. A few studies have targeted individual detections of the WNM in absorption to directly measure $T_s$ (e.g., Carilli et al. 1998, Dwarakanath et al. 2002, Murray et al. 2014), while many other surveys have estimated $T_s$ in the WMN from upper limits (i.e., $T_{k,max}$) or as line-of-sight averages in the presence of strongly absorbing CNM

gas (Mebold et al. 1982, Heiles & Troland 2003a, Kanekar et al. 2003, 2011, Roy et al. 2013b). Clear detection of broad and weak absorption lines from the WNM requires excellent spectral baselines and is best done using interferometers. The upgrade of the Karl G. Jansky Very Large Array (JVLA) resulted in a band-pass stability high enough to detect shallow ($\tau_0 \sim 10^{-3}$) and wide ($\delta v \sim 7$–$8\,\mathrm{km\,s^{-1}}$) absorption lines (Begum et al. 2010). In combination with HI emission from the Arecibo Observatory, Begum et al. (2010) identified individual absorption lines in the UNM regime with $T_s = 400$–$900$ K. Roy et al. (2013a,b) used the Westerbork Synthesis Radio Telescope, the Giant Metrewave Radio Telescope, and the ATCA for another deep HI absorption survey detecting the UNM. These studies emphasize the need for larger samples of interferometric detections of HI absorption at high sensitivity to constrain the fractions of gas in all HI phases.

The 21-SPONGE project (Murray et al. 2014, 2015, 2018) was one of the most sensitive absorption line surveys. It targeted 58 bright background sources, reaching a sensitivity of $\sigma_\tau < 1 \times 10^{-3}$ to detect HI absorption in all stable and thermally unstable phases. The HI absorption spectra were complemented with HI emission from Arecibo, and a streamlined, reproducible fitting and radiative transfer approach was used to constrain physical properties of HI.

While targeted HI absorption surveys are time consuming, large interferometric surveys of the Milky Way plane (CGPS, SGPS, VGPS, THOR) have had high enough spatial resolution to allow extraction of both HI absorption and emission spectra in the direction of background sources (Dickey et al. 2003, 2009; Strasser et al. 2007). For example, this approach enabled a large sample of ~300 absorption–emission pairs that was used by Dickey et al. (2009). While providing important constraints about the spatial distribution of the CNM, these interferometric surveys mainly used integrated properties because HI spectra within a few degrees from the plane are very complex.

Recent 21 cm HI absorption and emission surveys are summarized in **Supplemental Table 1**. From a subset of these surveys, we have compiled a catalog containing key observed properties of HI absorption in the Milky Way. The compilation, which we call BIGHICAT and describe in the **Supplemental Material**, combines publicly available spectral Gaussian decompositions of several surveys. In total, the BIGHICAT comprises 372 unique lines of sight and 1,223 Gaussian absorption components, providing $T_s$, peak $\tau$, and other properties. **Figure 3** shows the distribution of these lines of sight.

Supplemental Material >

### 4.3. HI Self-Absorption

Another manifestation of HI absorption is HI self-absorption (HISA), which occurs when cold HI lies in front of warmer background HI emission at the same velocity. HISA is not, strictly speaking, self-absorption—the two HI features are not cospatial, but they are cospectral. HI in the inner Galaxy, where velocities correspond to two distances, provides an ideal background for detecting foreground cold HI as HISA. Broadly, HISA is evident in two situations: high optical depth environments with a moderate background, such as molecular clouds (often referred to as HINSA; e.g., Li & Goldsmith 2003, 2012), and moderate optical depth CNM with a high-brightness background, such as the Galactic Plane (e.g., Gibson et al. 2005b). A prominent example of the latter type of self-absorption, the Riegel–Crutcher cloud, is shown in **Figure 4**. HISA has historically been used to study the structure and temperature of cold clouds (e.g., Heeschen 1955, Knapp 1974, Baker & Burton 1979), but its widespread presence became particularly clear with the high resolution afforded by interferometric Galactic Plane surveys (Gibson et al. 2000, 2005a; Beuther et al. 2020; Wang et al. 2020a,b).

An advantage of HISA over other observations of HI emission is that it clearly separates the CNM from the WNM. Whereas HI emission is usually dominated by the WNM, and the physical

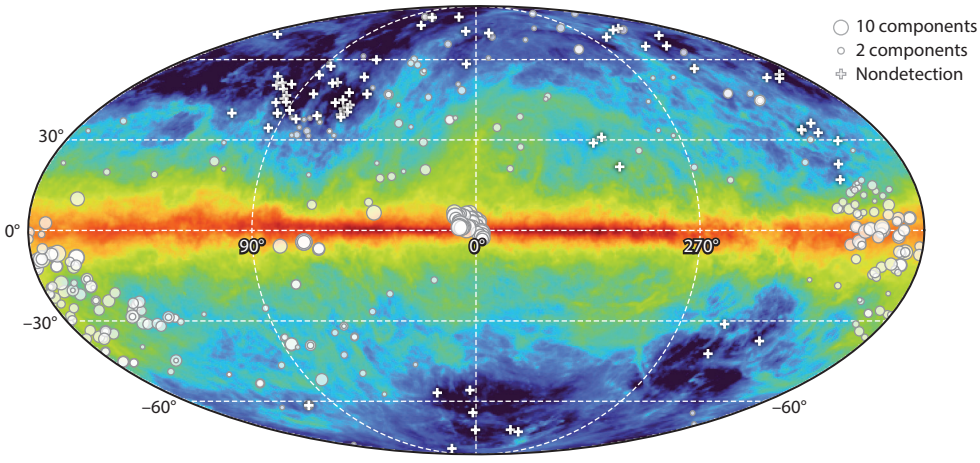


**Figure 3**

Compilation of HI absorption spectra from the BIGHICAT catalog overlaid on a map of HI emission integrated from −75 km s$^{-1}$ to +75 km s$^{-1}$ (Ben Bekhti et al. 2016). Nondetections are shown as crosses; detections are sized according to the number of absorption components. Coordinates are Galactic.

properties of the CNM are primarily studied in discrete lines of sight toward continuum sources (an HI-absorption "grid"), HISA can give continuous spatial sampling of the CNM. In practice, however, the efficacy of spatial recovery of the cloud properties ($N_{\rm H}$, $\tau$, and $T_{\rm s}$) is not trivial because variations in background HI emission can obfuscate the properties of the absorbing cold cloud.

Solving the radiative transfer equation (Equation 9) for HISA is even more complicated than for continuum absorption. We have to consider not only the continuum background, $T_{\rm c}$, but also the spin temperature and optical depth of all of the emitting and absorbing HI along the line of sight, including the foreground ($T_{\rm s,f}$, $\tau_{\rm f}$) and background ($T_{\rm s,b}$, $\tau_{\rm b}$), and the HISA feature itself ($T_{\rm s,HISA}$, $\tau_{\rm HISA}$). Therefore, the expected brightness temperature, $T_{\rm b}$, observed in the direction of a cold HISA structure is

$$\begin{aligned} T_{\rm b} \;=\; & T_{\rm s,f}\,(1-e^{-\tau_{\rm f}}) \\ & + T_{\rm s,HISA}\,(1-e^{-\tau_{\rm HISA}})\,e^{-\tau_{\rm f}} \\ & + T_{\rm s,b}\,(1-e^{-\tau_{\rm b}})\,e^{-(\tau_{\rm f}+\tau_{\rm HISA})} \\ & + T_{\rm c}\,e^{-(\tau_{\rm f}+\tau_{\rm HISA}+\tau_{\rm b})}. \end{aligned} \qquad 10.$$

All quantities except $T_{\rm c}$ are functions of radial velocity. Unlike continuum absorption, where the brightness temperature without any absorption can be easily measured adjacent to the source, for spatially extended HISA, $T_{\rm off}$ is usually estimated by interpolating over the absorption feature in velocity space. In all HISA observations, $T_{\rm s,HISA}$ and $\tau_{\rm HISA}$ are degenerate. Various approaches have been proposed to solve Equation 10 for $T_{\rm s,HISA}$ and $\tau_{\rm HISA}$ (Knapp 1974, Gibson et al. 2000), but an exact solution remains a challenge.

Despite the challenges of robustly solving for $T_{\rm s}$ with HISA, HISA provides a valuable probe of the transition zone between atomic and molecular gas in molecular clouds. Syed et al. (2020) and Wang et al. (2020b), for example, use the combination of traditional HI emission, HISA-traced gas, and CO-traced $H_2$ to measure the full hydrogen column density probability density function for giant molecular filaments. The addition of HISA-traced gas allows for an optical depth

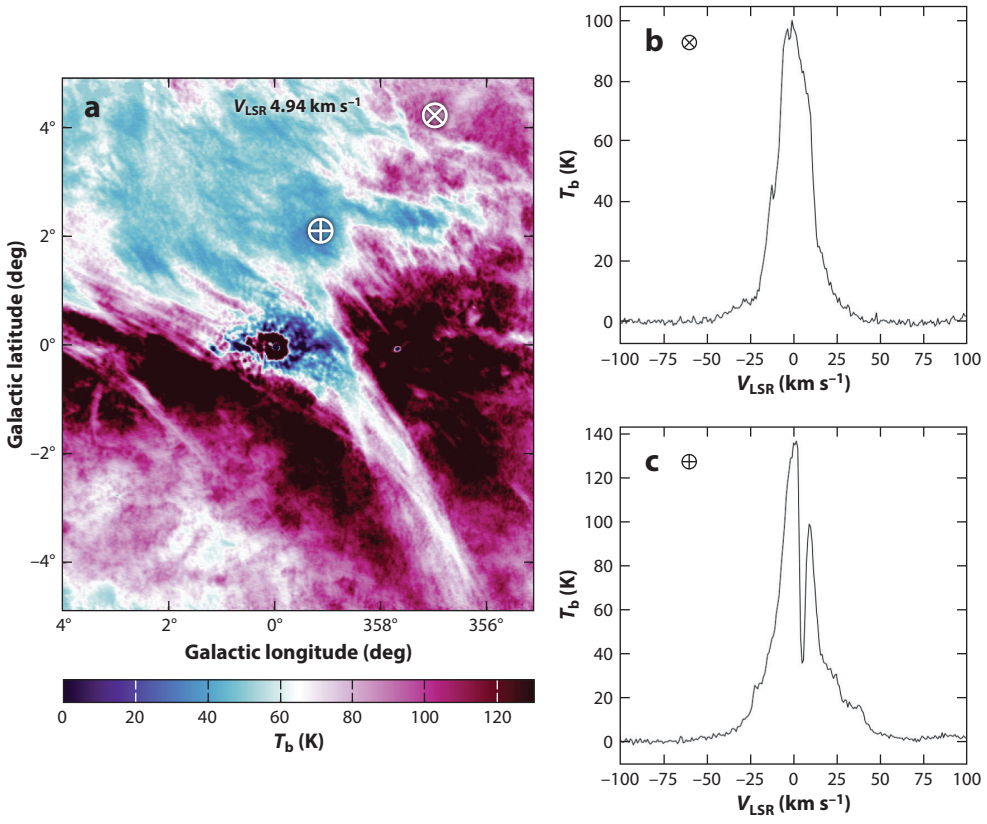


**Figure 4**

(*a*) HI self-absorption (HISA) in the Riegel–Crutcher cloud (McClure-Griffiths et al. 2006). (*b*) Spectrum at the position marked ⊗ in panel *a*. (*c*) Spectrum containing HISA at the position marked ⊕ in panel *a*. Figure adapted with permission from McClure-Griffiths et al. (2006).

correction to the HI emission, giving a more realistic total column density (subject to uncertainties in assumed values for $T_s$ and the fraction of foreground to background $T_b$). However, recent synthetic observations of SILCC-Zoom simulations have raised some concerns about the reliability of using HISA to measure $N_H$ (Seifried et al. 2022). Seifried et al. (2022) found that observations of HISA tend to underestimate the column density by factors of as much as 3–10 because HISA clouds rarely have a single temperature. Further studies of simulations will help guide observers in how best to incorporate HISA in $N_H$ measurements.

Perhaps the most important unique information that HISA gives is the spatially resolved kinematics of the CNM. To spatially resolve velocity gradients in the CNM from emission, observers have to separate the narrow-linewidth CNM from the pervasive broad-linewidth WNM. Spectral decomposition of complex HI emission profiles is generally not unique (see Marchal et al. 2019). CNM traced by HISA, on the other hand, is relatively easy to separate spectrally from the confusing WNM, making it useful for deriving velocity fields of CNM structures. Beuther et al. (2020) used this technique to show that the HISA-traced CNM around the infrared dark cloud G28.3 is kinematically decoupled from the denser gas as traced by $^{13}$CO and [CI]. It seems certain that, with the increased angular resolution and sensitivity of future surveys, HISA will be used more extensively.

## 5. THE NATURE OF HI IN THE MILKY WAY

While HI emission surveys have been invaluable in revealing detailed properties of the Galaxy's gaseous structure (for reviews, see Kulkarni & Heiles 1988, Dickey & Lockman 1990, Kalberla & Kerp 2009), perhaps the greatest advances in understanding the physics of Galactic HI over the last decade have come from studies of the physical properties, overall distribution, and structure of the absorbing HI. The absorbing HI, as we discuss in this section, represents mainly the CNM, with a very small fraction of absorption corresponding to the UNM and WNM. Because of observational limitations, our understanding of the nature of the CNM of galaxies comes almost exclusively from the Milky Way, yet the CNM is a critical step toward the formation of molecular clouds and therefore star formation. While many sensitive observations of HI absorption have been undertaken over the last 20 years, we are only beginning to understand CNM properties. Small samples still limit studies of the thermally unstable HI and a significant debate persists about what fraction of HI is in the UNM. As we move forward, the Milky Way will remain the key place for testing details of the multiphase physics, and we anticipate great advances in this area with upcoming large surveys.

Following the first astronomical observations of absorption and emission via the 21 cm transition of HI (Ewen & Purcell 1951, Muller & Oort 1951, Hagen et al. 1955), clear differences in the observed velocity structure between emission and absorption spectra were attributed to significant variations in the temperature and density of the gas along the line of sight (Clark 1965, Dickey et al. 1978). The distinction between HI structures of different phase (density and temperature) is still complex. As discussed in Section 4.2, this complexity comes from the often large overlap of different HI structures in the radial velocity space, as well as from the limitations posed by the observational sensitivity.

In the following subsections, we summarize what is currently known about the temperatures and mass fractions of the different HI phases. We use the BIGHICAT to examine environmental dependencies for the CNM.

### 5.1. Cold Neutral Medium Temperature

The CNM appears ubiquitous in the Milky Way. As shown in **Figure 3**, it is easily detected both at low Galactic latitudes, where absorption spectra often have multiple components, and at high Galactic latitudes, where spectra are simple, often with a single, low optical depth CNM feature. In the BIGHICAT, 306 of 372 directions show significant absorption in at least one component, and many HI absorption surveys, including 21-SPONGE, have shown a similarly high detection rate of HI absorption (more than 80%).

**Figure 5** uses entries from the BIGHICAT database, where individual velocity components were fitted with Gaussian functions and $T_s$ was derived to show the fraction of the total HI column density as a function of $T_s$. Murray et al. (2018) used synthetic HI spectra to demonstrate that the approach of fitting Gaussian functions to individual velocity components, in combination with radiative transfer calculations, is successful and complete at recovering the overall fraction of the HI mass that is in the CNM. **Figure 5*b*** can be compared with the numerical expectations shown in **Figure 2**. The observed HI gas as a fraction of total column density (or mass) peaks around 50–100 K, has a broad shoulder up to 500 K, and has an extended tail up to $T_s = 3{,}000$ K. Based on theoretical and numerical studies, the peak of the HI distribution corresponds to the CNM and has been observationally straightforward to detect (see the many references listed in Section 3.2; Dickey & Lockman 1990). Clearly, the (absorption) observed HI gas fraction is missing the WNM portion of the expected distribution. At this stage, the decline in the gas fraction of about $T_s = 500$ K is an observational limitation; even with long integrations, it has been very hard to detect the UNM and WNM in absorption (see Sections 5.4 and 5.5).

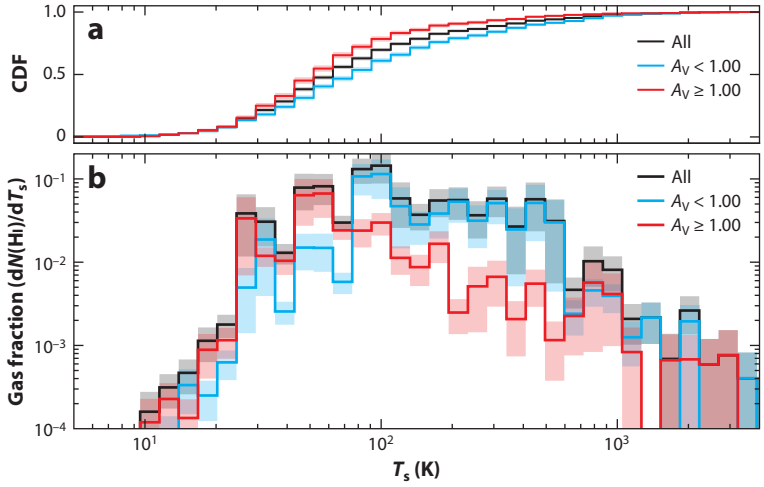


**Figure 5**

Fraction of the total column density detected as a function of spin temperature in the BIGHICAT HI absorption compilation. The overall fraction (*black*) is divided on the basis of visual extinction, $A_V$. The median temperature is $T_s \sim 50$ K. For high-extinction environments ($A_V \geq 1.0$; *red*), the temperature range observed in the cold neutral medium (CNM) is narrow and peaked at $T_s \approx 50$ K, whereas the low-extinction environments ($A_V < 1.0$; *blue*) show a broader range of CNM temperatures peaked closer to $T_s \approx 100$ K. (*a*) The $T_s$ cumulative distribution function (CDF) for each sample. (*b*) Uncertainties, calculated by bootstrapping more than 1,000 trials, are shown as shaded regions around the different histograms. The sample is incomplete in the range 500 K $\lesssim T_s \lesssim$ 4,000 K, where observational sensitivity limits the number of measurements.

The observed peak of CNM temperature distribution of ~50–200 K is largely in agreement with theoretical expectations for solar metallicity and radiation field (**Figure 2**), at low optical extinction. The BIGHICAT catalog is biased toward higher-latitude observations (due to the simplicity of HI spectral lines). As a result, ~41% of the BIGHICAT sample probes environments with $A_V <$ 0.2. **Figure 5*b*** shows gas fraction histograms obtained by splitting the sample into $A_V < 1$ and $A_V \geq 1$. The $A_V < 1$ subsample peaks at 80–100 K, while the $A_V \geq 1$ subsample peaks at a lower temperature (~50 K). This figure suggests that the broad CNM distribution comes from a combination of denser and more diffuse environments, with different physical environments resulting in a different range of temperatures.

Overall, we conclude that the observed CNM $T_s$ distribution is in line with theoretical expectations. It is broad, but the width appears to agree with expectations for the environmental dependence of $T_s$, as well as how local turbulent perturbations affect HI temperature. Building larger CNM samples to probe even more diverse ISM environments is highly important for the future.

Because it is expected that $H_2$ forms largely out of the CNM (e.g., Krumholz et al. 2009), an important question is: How do the CNM and $H_2$ temperatures compare? For example, Heiles & Troland (2003b) compared the CNM temperature with the $H_2$ temperature measured by FUSE for four directions where radio and UV sources were spatially close. They concluded that the $H_2$ and CNM temperatures do not agree. If we perform a similar analysis using the lines of sight in the BIGHICAT within ~1 deg of FUSE lines of sight from Shull et al. (2021), we find that the $H_2$ temperature, as measured through the lowest three rotational states ($J = 0, 1, 2$) of $H_2$, always lies between the minimum and maximum CNM temperatures along the line of sight. In three out of

four cases, the $H_2$ temperature is consistent with the temperature of the CNM component with the highest HI column density. Yet, as Heiles & Troland (2003b) noted, the temperatures derived for $H_2$ and HI are not directly comparable. The $H_2$ temperatures are calculated as a weighted mean over all velocity components because of the strong line saturation.

The mean excitation temperatures obtained by Shull et al. (2021) are $\langle T_{01} \rangle = 88 \pm 20$ K and $\langle T_{02} \rangle = 77 \pm 18$ K, which is very close to the CNM peak shown in **Figure 5**. For lines of sight with $E(B-V) > 0.5$ (which corresponds to $A_V > 1.5$) and $N_H > 10^{20.7}$ cm$^{-2}$, the $H_2$ temperatures decrease to 50–70 K. This value qualitatively agrees with **Figure 5** for $A_V > 1$, where $T_s$ shifts to lower temperature, supporting the idea that $H_2$ and the CNM are thermally coupled. Detailed comparisons of larger samples of HI velocity components with $H_2$ measurements remain as an important future task.

Homogeneous samples of other molecular species found in the diffuse ISM are starting to emerge, thanks to the Atacama Large Millimeter Array (ALMA) and Northern Extended Millimeter Array (NOEMA). For example, Rybarczyk et al. (2022) found that the molecular gas traced by $HCO^+$, $C_2H$, HCN, and HNC is associated only with HI structures that have an HI optical depth above 0.1, a spin temperature below 80 K, and a turbulent Mach number greater than 2. This result hints that not all CNM is useful for forming $H_2$, with only colder and denser CNM being thermally coupled to $H_2$.

## 5.2. Cold Neutral Medium Fraction

As the CNM is the key building block for $H_2$, constraining how the CNM fraction varies across the Milky Way is essential for understanding star formation efficiencies. The Millennium Arecibo survey showed that most of the 79 observed directions had a CNM column density (or mass) fraction below 0.3, with only a few lines of sight being dominated by the CNM (Heiles & Troland 2003b). In a few directions, this study found essentially no CNM and suggested that the CNM was destroyed in these directions by superbubbles. The study also observed that the CNM fraction increased with the total HI column density up to $\sim 1.2 \times 10^{20}$ cm$^{-2}$, and then leveled off. By comparing the WNM/CNM fraction at $|b| < 10$ deg, where lines of sight are mainly in the Galactic disk, with higher latitudes, Heiles & Troland (2003b) tested the hypothesis that the WNM fraction should be lower in the plane where thermal pressure is the highest but found no difference.

With larger samples and more sensitive data, observers are starting to find regions with CNM fractions that clearly deviate from typical ISM values. Murray et al. (2021) showed that the Galactic HI in the foreground of Complex C is particularly underabundant in the CNM. The whole region has a relatively low column density ($<10^{20}$ cm$^{-2}$ on average) and, despite narrow HI linewidths, shows a very low CNM fraction. Although the line-of-sight CNM fraction in the region differs from typical ISM fields, individual velocity components have similar $T_s$ and $\tau_0$, suggesting that this region is particularly quiescent. Murray et al. (2021) concluded that the region may be sampling an area that has not recently been disturbed by supernova shocks, leading its HI properties to be dominated by thermal motions rather than nonthermal, turbulent motions.

At the other extreme, observations near several giant molecular clouds (GMCs) have shown on average higher CNM fractions. For example, Stanimirović et al. (2014) investigated 26 HI absorption–emission pairs obtained in the direction of radio sources all in the vicinity of the Perseus molecular cloud. Their CNM fraction is in the range 0.2–0.5, with a median CNM fraction of 0.33 (in comparison to 0.22 from Heiles & Troland 2003b). Similarly, Nguyen et al. (2019) used 77 HI absorption–emission pairs in the vicinity of Taurus, California, Rosette, Mon OB1, and NGC 2264 and found a CNM fraction in the range $\sim$0.2–0.75, with a median value of 0.35. These results suggest a scenario in which a high CNM fraction is required for molecule formation, and

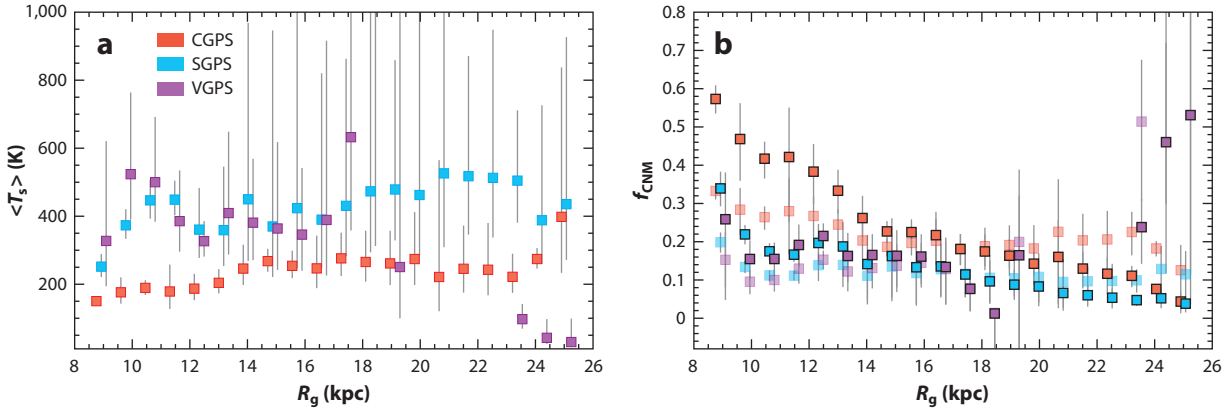


**Figure 6**

(*a*) Line-of-sight mean spin temperature $\langle T_s \rangle$ as a function of Galactic radius. The mean spin temperature is remarkably constant with Galactic radius in the outer Galaxy. (*b*) The implied cold neutral medium (CNM) fraction $f_{\rm CNM} = T_s/\langle T_s \rangle$ as a function of Galactic radius. The CNM fraction shown here is dependent on the assumed cold gas temperature. The dark points assume that $T_s$ varies with radius (based on Wolfire et al. 2003), and the lighter points assume $T_s = 50$ K. The Very Large Array Galactic Plane Survey (VGPS) data are affected by the Galactic warp, which takes the cold disk out of the survey area. Abbreviations: CGPS, Canadian Galactic Plane Survey; SGPS, Southern Galactic Plane Survey. Figure adapted with permission from Dickey et al. (2009).

GMCs are built up stage by stage—from WNM-rich gas to CNM-rich gas to molecular clouds. Another reason for the high CNM fraction around GMCs could be effective CNM accretion. Important future tasks will be to provide even denser grids of HI absorption sources and to map spatially and kinematically the distribution of the CNM in the vicinity of GMCs.

The line-of-sight mean spin temperature $\langle T_s \rangle$ (see also Section 5.3.2) can also be used as an indicator of the CNM fraction, where $f_{\rm CNM} = T_s/\langle T_s \rangle$, assuming $T_s$ as a representative cold cloud temperature. Dickey et al. (2009) compiled HI absorption–emission measurements in the Galactic Plane from the three Galactic Plane surveys (CGPS, SGPS, and VGPS) to measure $\langle T_s \rangle$ as a function of Galactic radius, $R$. These data are illustrated in **Figure 6**. The figure also shows the implied CNM fraction $f_{\rm CNM}$ with two representative assumptions of $T_s$: average cold temperatures from the heating and cooling models of Wolfire et al. (2003) ($T_s = 85$ K at $R = 8.5$ kpc to $T_s = 44.1$ K at $R = 18$ kpc) or a constant temperature of $T_s = 50$ K. If the typical cold cloud temperature decreases with Galactic radius, then $f_{\rm CNM}$ also decreases from ∼0.3 near the Solar Circle to less than 0.05 at $R \sim 25$ kpc. On the other hand, if we assume a flat $T_s$, as indicated by Strasser et al. (2007), the CNM fraction is remarkably flat to large radii. Clearly, the key observational element required to understand how the CNM fraction varies will be the typical cold cloud temperature. For completeness, we note that although these curves were calculated under the assumption of smooth circular rotation, which breaks down for individual lines of sight, the trends largely hold for the extended azimuthal (>70 deg) averages of the data shown in **Figure 6**.

HI emission surveys have also been used together with spectral decomposition to determine the fraction of gas in the CNM. For example, Kalberla & Haud (2018) found that for Galactic latitudes $|b| > 20$ deg the column density fraction of CNM was $25 \pm 5\%$ at local velocities, whereas Marchal & Miville-Deschênes (2021) estimated that in their high-latitude field the average CNM mass fraction was $8 \pm 6\%$, showing large excursions (up to ∼30%) along filamentary structures. Using a convolutional neutral network applied to the large-area GALFA-HI survey, Murray et al. (2020) found that the CNM fraction varies from <10% to ∼40%, depending on sky location.

In the full BIGHICAT compilation, the mean CNM fraction (of $T_s < 250$ K) along the line of sight is 0.35 and the median is 0.34. However, the BIGHICAT compilation is not uniform and contains numerous fields selected to be near the Galactic Plane or molecular clouds. Limiting the sample to $|b| > 20$ deg gives a mean of 0.31 and a median of 0.27 and might be more representative of the general ISM. The BIGHICAT CNM mass fraction is 40% if we assume that 50% of the total HI mass is detected only in emission (Murray et al. 2018).

## 5.3. Environmental Dependencies of Cold HI Properties

Theoretical models and numerical simulations show that the thermal pressure at which cold and warm HI coexist depends on key physical properties such as the ambient interstellar radiation field, metallicity, dust properties (composition, charge, efficiency, etc.), and interstellar turbulence. As these physical quantities vary across galaxies, we expect to see variations of HI gas properties. For example, photoelectric heating by dust grains may be enhanced in particularly dust-rich environments. Large-scale gradual metallicity variations are common across spiral galaxies (e.g., Shaver et al. 1983). Similarly, as shown in **Figure 1**, the CNM temperature should be affected by dust shielding in higher-$A_V$ regions. However, aside from several sporadic studies (some of which are listed in the previous sections), observational evidence of the regional diversity of CNM properties across the Milky Way is still lacking. This is largely due to the limited number of HI absorption spectra, as well as large measurement uncertainties in deriving key physical properties ($T_s, f_{CNM}$). With recent systematic observational and data analysis approaches and larger data samples, some interesting trends are starting to emerge.

**5.3.1. Does the CNM temperature vary across the Milky Way?** Over the years, sporadic observations have shown occasional directions with $T_s \sim 20$–$30$ K (Knapp & Verschuur 1972; Meyer et al. 2006, 2012). These temperatures are very low and are in the realm of what is usually found for molecular gas. Explaining theoretically such low temperatures requires the absence of photoelectric heating (e.g., Spitzer 1978, Wolfire et al. 2003) and/or significant shielding (Glover et al. 2010, Gong et al. 2017). On the other hand, many studies have noticed relatively uniform $T_s$ for the CNM in the inner and outer Galaxy (Strasser et al. 2007), in and around the Perseus molecular cloud, and in several additional GMCs (Stanimirović et al. 2014, Nguyen et al. 2019). Using line-of-sight integrated properties, Dénes et al. (2018) hinted at the existence of a slightly warmer $T_s$ close to the Galactic Center, as did Bihr et al. (2015) near the W43 "mini-starburst" star-forming region.

Theories of heating and cooling balance (e.g., **Figure 1**) show that regions with high dust column density (high $A_V$) have a low CNM temperature, whereas in regions with low $A_V$ the CNM temperature takes on a wide range of values (Bialy & Sternberg 2019, Bialy 2020). We used all available HI absorption spectra compiled in the BIGHICAT dataset to test whether $T_s$ depends on the optical extinction. As shown in **Figure 5**, the HI components in the directions with $A_V < 1$ occupy the higher-$T_s$ portion of the distribution relative to HI components in the directions with $A_V > 1$, which sample predominantly the lower-$T_s$ portion of the $T_s$ distribution. This result demonstrates that higher-$A_V$ regions provide more intense shielding, leading to lower $T_s$ (see also figure 10 of Kim et al. 2022). While this result is in line with theoretical expectations, the observed distributions of the cold HI are broader than theoretical expectations. This could be due to the presence of turbulence that spreads out the temperature distribution.

Clearly, these observations are just the beginning, and future HI surveys with larger samples of absorption lines are needed to confirm these trends. These results demonstrate the power of large HI absorption samples to depict, for the first time, differences in HI temperature distributions caused by the underlying physical conditions.

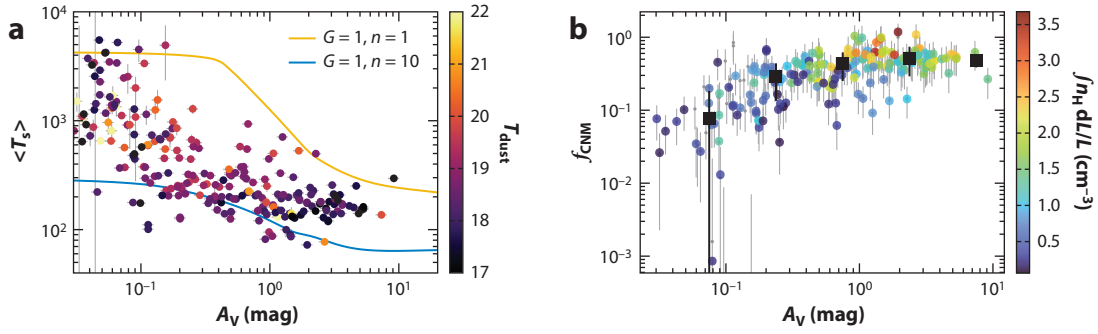


**Figure 7**

(*a*) The optical depth–weighted spin temperature from the BIGHICAT dataset as a function of optical extinction from Planck. Points are colored according to the dust temperature, and the lines are from the photodissociation region model presented by Gong et al. (2017). (*b*) The cold neutral medium (CNM) fraction from the BIGHICAT dataset as a function of optical extinction from Planck. The points are colored by mean volume density $\langle n_H \rangle$ (data are from the 3D dust map of Lallement et al. 2019). The mean points (*black squares*) show that the CNM fraction flattens at ∼60–80%. The HI absorption data probe arcsecond angular scales, while $A_V$ from Planck probes angular scales of ∼5′. The high-$A_V$ limit in this figure is not well defined, as HI spectra can be saturated and difficult to interpret. Model data kindly provided by M. Gong.

**5.3.2. What physical conditions are essential for setting HI properties?** The $T_s$ distribution shown in **Figure 5** suggests that the HI temperature depends on optical extinction. To investigate a physical origin of the dependence of temperature on extinction, **Figure 7*a*** shows the optical depth–weighted average spin temperature, $\langle T_s \rangle = \int \tau(v) T_s(v) dv / \int \tau(v) dv$, as a function of $A_V$. Both $\langle T_s \rangle$ and $A_V$ are line-of-sight quantities. The figure shows that cold HI exists over a very broad range of conditions: from very diffuse environments $A_V \sim 0.03$ all the way to $A_V \sim 10$. The latter value is often used to characterize dense molecular clouds (Snow & McCall 2006). However, the observed distribution is smooth, suggesting a continuous range of HI structures instead of well-segregated groups (e.g., diffuse atomic, diffuse molecular, translucent, dense molecular). Overplotted in **Figure 7** are two color lines showing predictions from the photodissociation region model from Gong et al. (2017) for particular input values $G \sim 1$ (i.e., solar UV radiation field) and $n = 1$–$10$ cm$^{-3}$. These lines nicely bracket the observed $\langle T_s \rangle$ values, showing that the local density plays a crucial role in constraining HI properties.

As discussed above, $\langle T_s \rangle$ is related to the CNM fraction along the line of sight, $f_{CNM}$,[1] as $\langle T_s \rangle \sim T_s / f_{CNM}$, so the trend of $\langle T_s \rangle$ shown in **Figure 7*a*** can reflect variations in the cold cloud temperature, $T_s$, or the CNM fraction, $f_{CNM}$. However, for $A_V > 0.2$ (**Figure 1**), the CNM temperature has a very narrow distribution (∼50 K). Assuming a well-constrained CNM temperature for $A_V > 0.2$, **Figure 7*b*** shows that $f_{CNM}$ increases with $A_V$ from ∼10% to ∼80%. The color of the points in **Figure 7*b*** shows the mean volume density along the line of sight, demonstrating that the lines of sight with higher $A_V$—and higher $f_{CNM}$—are those with the highest mean densities. We conclude that local density plays a crucial role in constraining the CNM fraction. Higher local density implies more shielding, as well as cooling, and therefore more CNM.

While some particular conditions could result in the HI being entirely CNM, this is not the case in the Milky Way. The mean points in **Figure 7*b*** show that the CNM fraction flattens at

[1]The values of $f_{CNM}$ shown in **Figure 7** are calculated using equation 18 of Kim et al. (2014). Uncertainties are calculated by varying the warm and cold cloud temperatures, as done by Murray et al. (2021). We find the same qualitative results if we take $f_{CNM}$ as $N|_{T_s<250\,K}/N_{LOS}$.

~60–80%. Some of the highest-$A_V$ directions certainly probe environments around dense molecular clouds, so the flattening of the CNM fraction at $A_V \sim 1$ could signify the transition of HI into $H_2$. However, as Stanimirović et al. (2014) pointed out, even lines of sight that probe deep inside the GMCs have a contribution from the WNM. The geometry and the level of mixing of the CNM and WNM are still not understood; it is not clear whether the WNM is located primarily in outer regions of the HI envelope, as theorized by McKee & Ostriker (1977), or whether the WNM is well mixed by turbulence. A priori, one might assume that WNM mixed into high-pressure molecular clouds would rapidly cool, but Hennebelle & Inutsuka (2006) showed that the dissipation of magnetic waves can provide substantial heating to maintain the WNM inside molecular clouds. It therefore seems unsurprising that the HI is not fully incorporated into the CNM in most environments and $f_{CNM} < 1$.

The low-$A_V$ end of **Figure 7** is also interesting, but poorly constrained by the observational data. Kanekar et al. (2011) noticed that lines of sight with column density greater than $2 \times 10^{20}$ cm$^{-2}$ had low optical depth–averaged spin temperature, which they interpreted as evidence of a threshold for CNM formation. Kim et al. (2014) suggested that, instead of a column density threshold, $A_V \sim 0.1$ may simply correspond to a characteristic length scale for CNM structures. Despite the larger sample in the BIGHICAT, the jury is still out on whether a column density threshold exists for CNM formation.

## 5.4. Unstable Neutral Medium Temperature and Fraction

It has been difficult to constrain the observational properties of HI at temperatures $T_s > 250$ K. Until recently, most estimates of the UNM temperature were made as upper limits from the linewidth-based kinetic temperatures of either emission or absorption. UNM mass fraction estimates made from HI emission give fractions between $28 \pm 11\%$ (Marchal & Miville-Deschênes 2021) and 41% (Kalberla & Haud 2018). Using upper limits to kinetic temperatures of HI absorption, Kanekar et al. (2003) found UNM fractions of 77% and 72% by mass for two lines of sight. By contrast, Begum et al. (2010) estimated 27% across five lines of sight, and Roy et al. (2013b) set a lower limit of ~28% mass fraction with values as high as 44%. The lower limit is based on the conservative assumptions that all detected CNM has $T_s = 200$ K and that all nondetected WNM has $T_s = 5{,}000$ K, and not on direct measurements of the absorbing and emitting properties of the unstable gas. Limits on the fraction of the medium in the unstable state based on spin temperature should be more robust, but they have been difficult to obtain because of the low optical depths inherent to the UNM and WNM.

Only a handful of observations have achieved the optical depth sensitivity required to measure $T_s$ in the UNM. For example, Heiles & Troland (2003b) detected 13 UNM components, giving an estimated column density fraction of 29% for spin temperatures measured out of the plane. The best estimates for UNM fraction have come from the 21-SPONGE survey (Murray et al. 2018), which conducted very deep HI absorption observations and was sensitive to HI with spin temperature up to ~4,000 K. This was not only the first statistically significant survey designed to detect low optical depth ($\tau \sim$ few $\times 10^{-3}$) broad lines; it also took exceptional care of observational biases introduced in the analysis method used to constrain HI spin temperature and recover the HI mass distribution. 21-SPONGE tripled the number of UNM components and found 20% of the total HI mass, and $41 \pm 10\%$ of the HI mass detected in absorption, to correspond to the UNM (Murray et al. 2018). The result agreed with the Heiles & Troland (2003b) sample and with the Begum et al. (2010) and Roy et al. (2013b) studies. Subsequently, a high-sensitivity survey (Nguyen et al. 2019) found a similar fraction.

A seemingly trivial, but important, distinction in the various observational and theoretical studies is the chosen boundary between the CNM and UNM. By combining several HI absorption

surveys in BIGHICAT, we have compiled the largest database of high-latitude ($b > 15$ deg) spin temperatures to search for a possible observational boundary between the CNM and UNM. We find no clear observational boundary, but we suggest that observers and theorists adopt the value of 250 K as a nominal boundary between the CNM and UNM simply to ease cross-comparison.

Driven largely by 21-SPONGE, the consensus seems to be pointing toward around 20–30% of the HI by mass being in the unstable phase. The result is similar to the HI emission UNM fractions (28% and 41%) derived by Marchal & Miville-Deschênes (2021) and Kalberla & Haud (2018), given the errors on those estimates. The observed UNM fraction agrees well with the mass fraction at UNM temperatures from the TIGRESS and SILCC numerical simulations shown in **Figure 2** (Kim & Ostriker 2017, Rathjen et al. 2021).

The spatial distribution of the UNM is currently uncertain. For example, Murray et al. (2018) noticed that the highest Galactic latitudes are dominated by WNM, while the CNM and UNM dominate low Galactic latitudes. However, the Gaussian decomposition is least reliable at low latitudes. On the other hand, Kalberla & Haud (2018), who studied UNM via HI emission lines, concluded that CNM structures are surrounded by the UNM, which often has filamentary morphology. As shown in **Figure 7**, from the BIGHICAT catalog we see that regions with $A_V > 1$ have slightly colder peaks $T_s$, due to increased shielding, and also exhibit less UNM (at $T_s \sim 200$–$600$ K) relative to the more diffuse HI environments with $A_V < 1$. The lower UNM fraction is likely caused by more pronounced dynamical processes at low $A_V$ and more shielding at high $A_V$, in agreement with suggestions by Wolfire (2015). Future observational constraints of the UNM spatial distribution will be very important to help determine the processes that drive HI out of equilibrium.

## 5.5. Warm Neutral Medium Temperature and Fraction

As the WNM usually dominates HI emission spectra, its properties are sometimes derived purely from HI emission data. Kalberla & Haud (2015, 2018) decomposed the HI4PI survey spectra into Gaussian components and selected three phases (CNM, UNM, WNM) based on the width of the Gaussian functions. They found that the WNM was smoothly distributed with a mass fraction of ~32%. Similarly, Marchal & Miville-Deschênes (2021) decomposed the high-resolution $12 \times 12$ deg GHIGLS field into Gaussian components and found that 64% of the HI mass is in the WNM. However, the standard deviation of that value is relatively high (35% of the median value). By comparing HI with extinction data, they estimated the WNM temperature as $T_k = (6.0 \pm 1.3) \times 10^3$ K.

Absorption–emission pairs are required in order to robustly estimate the excitation temperature of the WNM, without corruption by turbulent motions. High-sensitivity interferometric HI absorption observations have been used to measure the WNM temperature. For example, Carilli et al. (1998) measured $T_s = 5{,}500$–$8{,}700$ K in the direction of Cygnus A. Dwarakanath et al. (2002) and Kanekar et al. (2003) found lower values of 3,000–3,600 K.

The very sensitive HI absorption survey 21-SPONGE detected a handful of components with $T_s > 1{,}000$ K (e.g., <10% by number in Murray et al. 2015). To further improve the sensitivity to shallow, broad absorption features, Murray et al. (2014) employed a spectral stacking analysis on one-third of the survey data and detected a pervasive population of WNM gas with $T_s = 7{,}200^{+1{,}800}_{-1{,}200}$ K. Murray et al. (2018) comfirmed this result using data from the entire 21-SPONGE survey, where residual absorption was stacked and binned on the basis of residual emission, demonstrating the existence of a significant absorption feature with a harmonic mean $T_s \sim 10^4$ K.

The range of predicted kinetic temperatures for the WNM from the most detailed ISM heating and cooling considerations is $T_k \sim 5{,}000$–$8{,}800$ K (Wolfire et al. 2003). If the HI is only collisionally excited, as shown by Kim et al. (2014), then this range implies $T_s \sim 1{,}000$–$4{,}000$ K (see

figure 2 of Wolfire et al. 2003). However, when the common prescription is used to account for the Ly-α flux, it is expected that $T_s \sim 3{,}500$–$5{,}000$ K. The Murray et al. (2014) and Carilli et al. (1998) results are significantly higher than predictions from standard ISM models based on collisional HI excitation. As shown in **Figure 5**, even all combined HI absorption measurements together are not enough to detect the WNM peak of the HI gas distribution, suggesting that the WNM spin temperature is likely higher than standard analytical and numerical predictions. Another problem could be the implementation of the $T_k$-to-$T_s$ conversion and the use of a constant Ly-α flux. In a recent study by Seon & Kim (2020), which used a multiphase model and tracked photons originating from HII regions to produce the Ly-α radiation field, the Ly-α flux was strong enough to bring the 21 cm spin temperature of the WNM close to the kinetic temperature. This encouraging result demonstrates that a careful treatment of Ly-α photons needs to be incorporated into numerical simulations, instead of the commonly used uniform Ly-α flux.

In summary, the WNM remains difficult to detect in absorption and requires long integration times or stacking analyses. The detection difficulty likely stems from the possibility that it has a higher excitation temperature than what was expected. Future surveys of HI absorption will be essential to probe spatial variations of the WNM temperature via stacking. Constraining methods that use Gaussian decomposition to separate HI phases using simulated data will be essential, as studies of external galaxies rely on this method exclusively.

## 5.6. The "Dark" Neutral Medium

The transition from HI to $H_2$ is a critical step in the evolution of galaxies. The efficiency with which this transition occurs appears to influence star formation efficiency globally. While the transition from HI to $H_2$ is extremely important, it is also not easy to study. $H_2$ is impossible to observe directly in typical star-forming conditions (Carilli & Walter 2013). CO is traditionally used as a proxy for $H_2$, but because it cannot self-shield, it is easily dissociated. In the dense conditions of star-forming molecular clouds, $H_2$ and dust shield CO so that it is readily detectable, but in the early stages of the atomic-to-molecular transition, CO is not observed. At the same time, the CNM that goes on to make $H_2$ is studied via absorption measurements that are largely limited to lines of sight in the direction of background sources. Excluding the dominant tracers of CO and HI, how do we find gas in its transition from HI to $H_2$?

The Fermi $\gamma$-ray telescope and the Planck telescope independently discovered a component of so-called dark gas, not detectable by HI or CO but inferred by its excess $\gamma$-ray emission and dust opacity (Grenier et al. 2005, Ade et al. et al. 2011). Astonishingly, the dark gas mass seems to be between 20% and 50% of the total HI and CO gas detected in the Solar Neighborhood. It was thought that this might be a vast reservoir of transition gas, caught between its purely atomic and self-shielding molecular states. The discovery prompted a flurry of research into whether the dark gas was primarily optically thick atomic gas or primarily CO-dark molecular gas (e.g., Fukui et al. 2014, 2015; Lee et al. 2015; Murray et al. 2018; Sofue 2018; Nguyen et al. 2019).

Indirect tracers are often used to resolve the nature of dark gas. For example, Fukui et al. (2014, 2015) assumed that, if dust and neutral gas are well mixed and the specific dust opacity is constant, the HI optical depth and spin temperature can be approximated from the observed Planck dust properties. Under these assumptions, they estimated that the HI optical depth must exceed one along most local lines of sight but that low-resolution data missed significant unresolved dense gas. Conversely, Lee et al. (2015) used direct measurements of HI absorption to show that in the Perseus molecular cloud fewer than 20% of lines of sight show $\tau > 1$. Murray et al. (2018) revisited this problem using some of the techniques of Fukui et al. (2015) applied to higher angular resolution GALFA-HI data. They found that the HI is largely diffuse at high latitudes down to 4 arcmin scales and that the lower angular resolution observations are not missing optically

thick HI. Nguyen et al. (2018) showed that the HI opacity effects become important only above $N_{HI} > 5 \times 10^{20}$ cm$^{-2}$.

Meanwhile, several studies have investigated alternative molecular gas tracers ($HCO^+$ and OH) instead of CO. Liszt et al. (2018) observed $HCO^+$—known to trace $H_2$ even in diffuse environments—in addition to CO toward 13 background sources in the direction of the Chameleon cloud. Whereas CO emission was detected in only 1 of these directions, $HCO^+$ absorption was detected in 12 of the 13 directions, and the $H_2$ column densities inferred from $HCO^+$ explained the discrepancy between the column densities derived from $\gamma$ rays and dust emission with those estimated from HI and CO. While Liszt et al. (2018) found that optically thick HI could contribute to the dark gas in several directions, their results showed that the dark gas could be accounted for primarily by dark molecular gas rather than dark atomic gas (although Hayashi et al. 2019 presented a contradictory view that Chameleon has more optically thick HI rather than CO-dark $H_2$). Independently, Nguyen et al. (2018) showed that the OH could be used as a proxy for $H_2$ over a broad range of column densities and that optically thick HI is not a major contributor. In the end, it seems that a combination of factors, including a small amount of optically thick HI (~10–30% increase in column density), evolution of dust properties, and CO-dark molecular gas, can resolve the dust opacity excess.

## 6. CHARACTERIZING THE STRUCTURE OF HI ON ALL SCALES

The morphology of the HI in the Milky Way is studied primarily through HI in emission. Therefore, our knowledge of structure has been dominated by the WNM. Observational advances with spatial and spectral resolution over the past 20 years have started to reveal some hints about the CNM structure. Extending our understanding of the statistical thermal properties of the two stable phases to an understanding of the differences in morphology of the Galaxy's structure in the HI phases is still underway.

The structure of HI in emission can be characterized in two ways: deterministic and scale-free. Through ever-improving observational data, supported by numerical simulations (e.g., Hill et al. 2018, Kim & Ostriker 2018), a picture has developed of the HI gas cycle in which the diffuse, scale-free HI is repeatedly ordered by large-scale compression into dense, often filamentary and magnetized (McClure-Griffiths et al. 2006), deterministic structures that catalyze cooling (Dawson et al. 2011) and may drive turbulence. Deterministic structures are those that likely originate from a specific event or series of events; of these, the most common are the shells, bubbles, and chimneys that dominate the HI sky on angular scales between one and hundreds of degrees (Heiles 1979, 1984; Hu 1981; McClure-Griffiths et al. 2002; Ehlerová & Palouš 2005).

### 6.1. Deterministic Structure: From Bubbles and Shells to Clouds, Filaments, and Chimneys

While some of the HI shells observed in the Milky Way are clearly associated with relics of massive stars (e.g., Normandeau et al. 1996, McClure-Griffiths et al. 2001), many of the largest HI shells have not been clearly connected to their parent stars. In fact, HI shells are rarely observed around currently active star-forming regions or even young supernova remnants. It seems that the HI shells are more often associated with larger, older objects, although there are some notable exceptions, such as GLIMPSE bubble N107 (Sidorin et al. 2014).

Identifying HI shells in the Milky Way is not easy. Until recently, most shells had been cataloged manually (Heiles 1979, 1984; McClure-Griffiths et al. 2002). Some attempts had been made to catalog shells semiautonomously (e.g., Ehlerová & Palouš 2005), with varying success. Issues affecting the success of automated searches relate to the velocity ambiguity of the inner Galaxy,

the prevalence of arcs or shell-like features even in turbulent data (a quick look at terrestrial clouds can confirm!), and complex overlapping structures. Most recently, Ehlerová & Palouš (2013) refined automated shell searches with requirements for completeness of the shell, velocity widths, and so forth. The resulting catalog from the LAB survey has 333 entries, distributed across the sky. Considering only shells outside the Solar Circle, the fraction of the disk's surface area covered by shells drops from ∼80% at the Solar Circle to ∼10% at 15 kpc. Apart from a handful of newly identified shells, research on HI shells has largely stagnated over the last decade. Progress has been limited partly by the lack of distances to HI structure and the difficulty in defining 3D structures. This is set to change in the coming years, with 3D dust maps helping to overcome problems with velocity ambiguities. Despite the difficulties in robustly identifying HI shells, they do have important roles in the evolution of HI structure and density.

The various observational studies published on HI supershells throughout the late 1990s and 2000s made it clear that the role of supershells is to order the diffuse HI into large-scale, filamentary structures visible throughout the Galactic Plane. Does the HI also cool within these structures? Simulations have shown that supershells sweep up the warm, ambient medium into dense, structured filamentary walls where the gas can cool to form CNM and molecular clumps (Koyama & Inutsuka 2000, Mac Low et al. 2005, Hopkins et al. 2012). From an observational perspective, this role is less well documented, although there have certainly been examples of supershells with associated molecular gas (e.g., Fukui et al. 1999, Dawson et al. 2008). McClure-Griffiths et al. (2003) found clumps of narrow-linewidth HI in the walls of a large supershell, suggesting that the structures were formed by Rayleigh–Taylor instabilities. Both Knee & Brunt (2001) and Moss et al. (2013) used HISA to show that the walls of two supershell structures were dominated by cold gas. The most comprehensive analysis of supershells as collectors and coolers of gas was produced by Dawson et al. (2011), who showed that within two supershells the walls were dominated by cold gas with estimated temperatures and densities of $T_k \sim 100$ K and $n_H \sim 10\ \mathrm{cm}^{-3}$. Comparing the walls with the surrounding medium, they found statistically significant indicators of narrow linewidths consistent with enhanced CNM fraction as well as molecular fraction.

**6.1.1. Filamentary structures.** Feedback events, like those observed in supershells, indicate that star formation helps establish the large-scale structure of the HI that may ultimately be devolved to smaller scales. Much of that large-scale structure after the star formation tracers are gone is filamentary. For example, Soler et al. (2020) used the THOR survey at 40 arcsec angular resolution to show that within the Galactic Plane the HI has a filamentary nature, with the filaments predominantly aligned with the Galactic Plane. In some places where star formation appears to have been active, the filamentary structure abruptly switches direction to out of the plane. Extending this research across the Galactic disk, Soler et al. (2022) showed that in the outer Galaxy the filamentary HI structures are predominantly parallel to the Galactic Plane and that inside the Solar Circle they are mostly perpendicular to the plane or without a preferred orientation. Their interpretation is that the filaments show the imprint of supernova feedback in the inner Galaxy and Galactic rotation and shear in the outer Milky Way.

Observationally, distinguishing the characteristic morphology of the CNM from that of the WNM has been difficult because the large linewidth and diffuse character of the WNM blur structure within position–position–velocity cubes of HI emission. The morphology of the CNM, with its generally lower brightness temperatures and narrow linewidths, is easily obscured within spectral channels dominated by warm gas. But spectacular examples of discrete, cold features that appear cloudlike or filamentary abound. For example, the very local Leo cold cloud's exceptionally narrow velocity width indicates a kinetic temperature of between 11 and 20 K (Peek et al.

2011, supported by absorption measurements from Murray et al. 2018). Recent research using a combination of spectral resolution, angular resolution, and sensitivity afforded by the GALFA-HI survey has revealed small-scale, narrow-linewidth, fibrous structures (Clark et al. 2019). The inference that the fibrous structures are cold has been confirmed through various techniques, including correlation with NaI absorption (Peek & Clark 2019), convolutional neural network CNM separation (Murray et al. 2020), and dust-to-gas comparison (Kalberla et al. 2020). All three papers (Peek & Clark 2019, Kalberla et al. 2020, Murray et al. 2020) hint that the morphology of the CNM, as observed in emission, is distinct from that of the WNM. Dense grids of HI absorption spectra, as well as new techniques that perform spectral decomposition of HI emission to separate the WNM and CNM by using HI absorption data as learning templates (e.g., Murray et al. 2020), will be important for further characterization of the CNM morphology.

**6.1.2. Disk–halo clouds.** The familiar paradigm that supershells can drive hot gas and metals is clearly illustrated by many examples of HI supershells that completely disrupt the HI disk (Normandeau et al. 1996, Heiles 1998, McClure-Griffiths et al. 2002, Pidopryhora et al. 2007, Dawson et al. 2008). They also seem to contribute to categorizing the structure of the disk–halo interface region into so-called clouds or cloudlets. In their review of HI in the Milky Way, Dickey & Lockman (1990) asserted that the concept of HI clouds is not a useful one. Indeed, a quick examination of HI emission images (such as those shown in the movie in the **Supplemental Material**) will confirm that assertion—how could any of this structure be defined as a cloud? Nevertheless, this description of HI has persisted in the ISM lexicon. Despite its general appearance, a few examples of warm HI in the disk–halo interface region can reasonably be described as cloudlike. Lockman (2002) identified an unexpected population of HI structures that are clearly discrete and bounded and therefore cloudlike. These parsec-scale clouds are near the tangent point of the inner Galaxy, where small offsets from circular velocity place them at nearly forbidden velocities. Subsequent studies have suggested that the disk–halo cloud population is not ubiquitous throughout the Milky Way (Stanimirović et al. 2006; Stil et al. 2006; Ford et al. 2008, 2010; Pidopryhora et al. 2015) but may instead be a result of ISM structure driven in some indirect way by star formation. Ford et al. (2010) connected the clouds with broken remnants of shells and supershells driven away from the disk.

Supplemental Material >

## 6.2. Linking Magnetic Fields to HI Structure

Although the link between atomic gas and magnetism is not necessarily intuitive, early research on the correlation of starlight polarization with many large-scale local HI structures, such as Loop I and the Orion–Eridanus bubble (Heiles 1997), indicated that magnetic fields are associated with the morphological structure of HI. Using observations of Zeeman splitting of the HI line in absorption, Heiles (1989) showed that, for a sample of lines of sight through local supershells, the magnetic field strengths were larger than the typical ISM values. The Zeeman studies and the correlation of starlight polarization angle with HI loops imply that the magnetic field and HI were costructured through a common formation mechanism, such as supershells (Heiles 1989, 1998).

HI Zeeman research culminated with the Millennium Survey of HI absorption, which yielded 69 measurements on arbitrary lines of sight with magnetic field strengths of $|B_{\rm LOS}| \leq 10$ μG (Heiles & Troland 2004, 2005). Through comparison of $|B_{\rm LOS}|$ with column density, the survey showed that the field strengths are not consistent with flux freezing, as is typically found in molecular clouds (Crutcher 1999). The technical challenges of HI Zeeman observations have limited the extensive application of Zeeman research and large-scale conclusions about the connection of magnetic field strengths with the structure of the neutral medium.

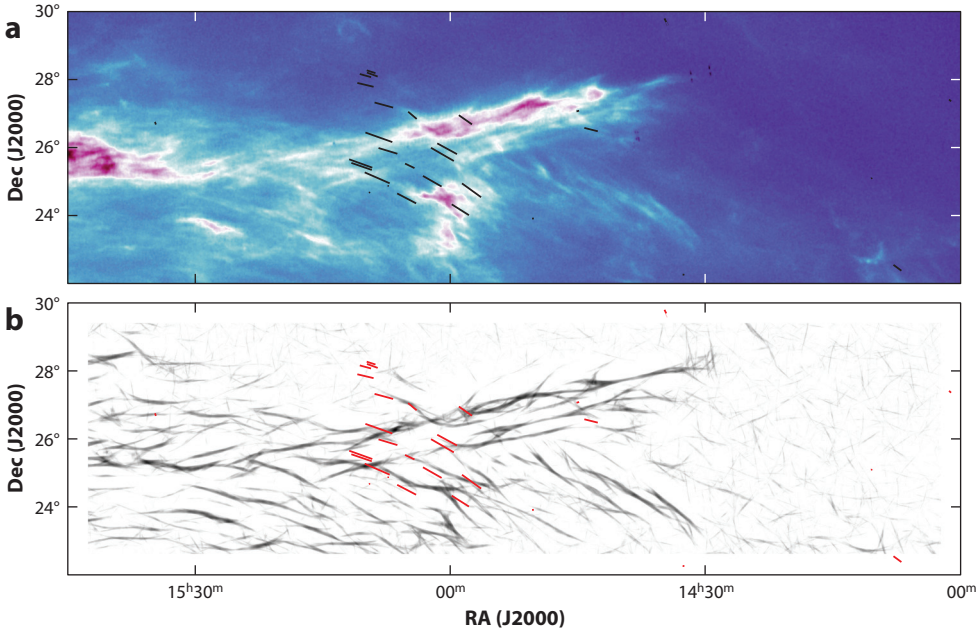


**Figure 8**

(*a*) HI image at $v = -7$ km s$^{-1}$ from GALFA-HI (Peek et al. 2018), showing fibrous structure overlaid with starlight polarization vectors (Heiles 2000). (*b*) Rolling Hough transform (Clark et al. 2014) backlit image of filamentary HI structure from the same HI data, overlaid with the same polarization vectors.

Over the last decade, a growing body of research has indicated that HI structure is linked to magnetic field structure, as traced by starlight and dust polarization (e.g., McClure-Griffiths et al. 2006, Clark et al. 2014, Clark & Hensley 2019). **Figure 8** shows an example of an HI velocity channel image with the fibrous structure emphasized by the rolling Hough transform overlaid with starlight polarization. So far, most of the observational evidence linking HI structure to magnetic fields has focused on the CNM. Clearly, the HI Zeeman measurements, by nature of tracing absorption, exclusively measure the CNM. This connection with the CNM was borne out in studies by Clark et al. (2019) and Kalberla et al. (2020), who showed that the magnetically correlated fibrous structure of the HI is dominated by narrow linewidths. Similarly, the structure of the cold Riegel–Crutcher HISA cloud (see Section 4.3) has outstanding agreement with starlight polarization (McClure-Griffiths et al. 2006). Extending to the whole sky, Kalberla et al. (2021) found remarkably good agreement between the far-infrared polarization angle and the HI filament orientation angle for velocity widths of 1 km s$^{-1}$, but for larger velocity widths, the agreement disappeared. The conclusion seems to be that HI filamentary structure is cold and magnetically dominated, with the field orientation parallel to the filaments.

Turning the technique around, fibrous HI structure has been used as a proxy for direct observations of magnetic fields, adding a velocity dimension to the observational technique of dust polarization. Clark & Hensley (2019) performed a full-sky decomposition of the fibrous HI that led to a velocity resolved projection of the plane-of-sky magnetic field. An alternative method proposed by González-Casanova & Lazarian (2017) and Yuen & Lazarian (2017) exploits the connection between turbulent motion and the magnetic field by using gradients of the velocity amplitude, which are expected to be perpendicular to the magnetic field direction, to trace the magnetic field orientation. Hu et al. (2021) employed another technique focusing on

the structure function of simulated HI to reveal both the magnetic field direction and its strength. The underlying correlation of HI structure and magnetic fields is an area of great activity and will likely develop rapidly over the coming years.

The fact that the two ISM elements—magnetic fields and the CNM—correlate so well suggests either that the magnetic field is dynamically important in setting the structure of HI in many environments or that the same dynamical events (e.g., supershells) that help produce CNM also enhance magnetic field strengths. While most observations linking magnetic fields and HI have focused on starlight or dust polarization as the tracer of magnetic field, several recent studies have used Faraday rotation of radio continuum as the magnetic field tracer (Van Eck et al. 2019, Bracco et al. 2020, Turić et al. 2021). Radio continuum studies may help break the bias of magnetic fields traced in cold gas by dust, instead showing magnetic fields in the warm, ionized medium probed by Faraday rotation. However, recent low-frequency radio polarimetric observations of Faraday rotation have generally found a morphological association with cold HI structures. Campbell et al. (2022) used midfrequency radio polarization Faraday rotation to show, for the first time, that the HI appears clearly connected to the warm ionized medium via a common magnetic field. While they consider whether a compressive event triggered the connection between the HI and the magnetic field, they cannot definitively conclude that it did. Future studies of Faraday rotation and HI will be important to reveal whether magnetism is as crucial to the structure of the WNM as it is to the CNM.

## 6.3. Statistical Description of the HI Distribution

Statistical studies provide an important and complementary way to describe and characterize complex, scale-free structure observed in high-resolution HI images. As interstellar turbulence is known to be ubiquitous throughout the ISM and largely responsible for the HI distribution in galaxies (e.g., Elmegreen & Scalo 2004), statistical descriptors of HI are important for constraining the drivers and the nature of interstellar turbulence. In addition, HI turbulence constraints are essential for understanding the process of molecular cloud formation and evolution, as studies of molecular clouds (e.g., Hennebelle & Falgarone 2012) show that most of the turbulent energy is injected from outside.

Turbulence can be driven by many energy sources that operate on different spatial scales. The key candidate is stellar feedback—a term used to express the combined effect of protostellar jets, stellar winds, photoheating, and supernovae (Offner & Arce 2014, Grisdale et al. 2017). Turbulent drivers operating mainly on larger spatial scales include gravitational instabilities (Elmegreen et al. 2003, Krumholz & Burkhart 2016), thermal instabilities (Kritsuk et al. 2007, Kim & Kim 2013, Iwasaki & Inutsuka 2014), and magnetorotational instabilities (Piontek & Ostriker 2004, 2005, 2007). However, clear observational signatures of different drivers of turbulence are still lacking, partly because of the need for an extremely high spatial dynamic range (from a few parsecs to many kiloparsecs).

Many different statistical approaches have been used on HI observations to characterize complex structure. Some of these approaches have been summarized by Elmegreen & Scalo (2004) and Scalo & Elmegreen (2004). Here, we focus on the SPS of HI as one of the common tools used to analyze HI emission, with the goal of compiling published results and pulling together some common trends.

In the presence of turbulence, the 2D SPS of HI intensity or column density fluctuations is expected to have a single or double power-law functional form (Scalo 1987). The SPS of a 2D image, $I(\mathbf{x})$, is defined as

$$P(k) = \int\int \langle I(\mathbf{x})I(\mathbf{x}')\rangle \exp^{i\mathbf{L}\cdot k}\, d\mathbf{L}, \qquad 11.$$

where $k$ is the spatial frequency and $\mathbf{L} = \mathbf{x} - \mathbf{x}'$ is the distance between two points in the image. The power-law slope of the SPS, $P(k) \propto k^{\gamma}$, derived from 2D HI images reflects contributions from the underlying 3D velocity and/or density fluctuations (Lazarian & Pogosyan 2000). Theoretically, the SPS can illuminate the spatial scales at which energy is injected or dissipated, as well as the mechanisms by which that energy cascades from large to small scales or vice versa.

Practically, however, the interpretation of SPS results is complex because of many observational and theoretical effects. The SPS slope depends on the line-of-sight complexity (e.g., multiple HI structures in the same direction), the multiphase nature of the HI, and optical depth effects. Furthermore, the disk geometry and the HI scale height can result in a transition between 2D and 3D turbulence, producing breaks in the SPS. Recent studies have shown that the interpretation of SPS breaks can be significantly affected by telescope instrumental effects (beam and noise) and by the multiphase nature of the medium (Koch et al. 2019, Körtgen et al. 2021). Similarly, separating density and velocity fluctuations from observed intensity fluctuations requires careful consideration. The way to do so, by varying the width of velocity channels (Lazarian & Pogosyan 2000), has recently been updated with a more complex treatment (Yuen et al. 2021). However, some debate remains. Clark et al. (2019) and Kalberla et al. (2016) suggested that HI intensity fluctuations observed at different velocities are phase dependent, with narrow velocity channels being dominated by the CNM and causing the HI SPS slope to be shallower than what is found for the integrated intensity images. Finally, it is not clear whether the SPS of HI emission is sensitive in distinguishing between different turbulent modes within a multiphase medium.

From the observational point of view, although many measurements of the HI SPS exist, most studies employed different analysis techniques, resulting in heterogeneous samples that are hard to compare and making it difficult to search for spatial variations of turbulent properties with interstellar environments. Early HI SPS studies by Crovisier & Dickey (1983) and Green (1993) fitted a single power law with indices of $-3.0$ and $-2.8$, respectively. Subsequent large-area (many degrees across) HI maps have also been used to calculate a single SPS. As many studies of HI SPS showed no evidence for turnover on large spatial scales, the interpretation has been that HI turbulence in the Milky Way is being driven on scales larger than the size of individual HI structures (e.g., Pingel et al. 2013, 2018). This is somewhat puzzling, considering the existence of many star-forming regions and supernovae in the disk, which we expect would modify turbulent properties of HI.

**Figure 9** compares values of the HI SPS slope from the literature. We note that all of these measurements were obtained from HI images integrated over a range of velocity channels that roughly correspond to the local HI ($\pm$20–40 km s$^{-1}$) and likely represent estimates of density fluctuations (based on Lazarian & Pogosyan 2000, Yuen et al. 2021). The figure also shows the application of the rolling SPS analysis to the entire region observed by the GALFA-HI survey from A.K. Mittal, B.L. Babler & S. Stanimirović (manuscript in preparation). The rolling SPS method, introduced by Szotkowski et al. (2019), calculates SPS locally by rolling a spatial kernel across an image. This method allows for a consistent handling of instrumental effects.

The GALFA-HI survey covers $\sim$13,000 deg$^2$ and includes a region in the inner Galaxy, a region in the outer Galaxy, and some high-latitude HI. The SPS slope, calculated over the angular range of scales from 1.5 deg to 16 arcmin, varies between $-2.6$ and $-3.5$. Close to the Galactic Plane, $|b| < 10$ deg, the SPS slope is the steepest, while at higher Galactic latitudes the SPS slope gradually becomes shallower, reaching approximately $-2.7$ at $|b| > 70$ deg (**Figure 9**). While the gradual change in SPS slope with Galactic latitude cannot be explained with optical depth effects, it becomes less significant when the HI column density is corrected for the difference in the line-of-sight length caused by the plane-parallel geometry of the HI disk.

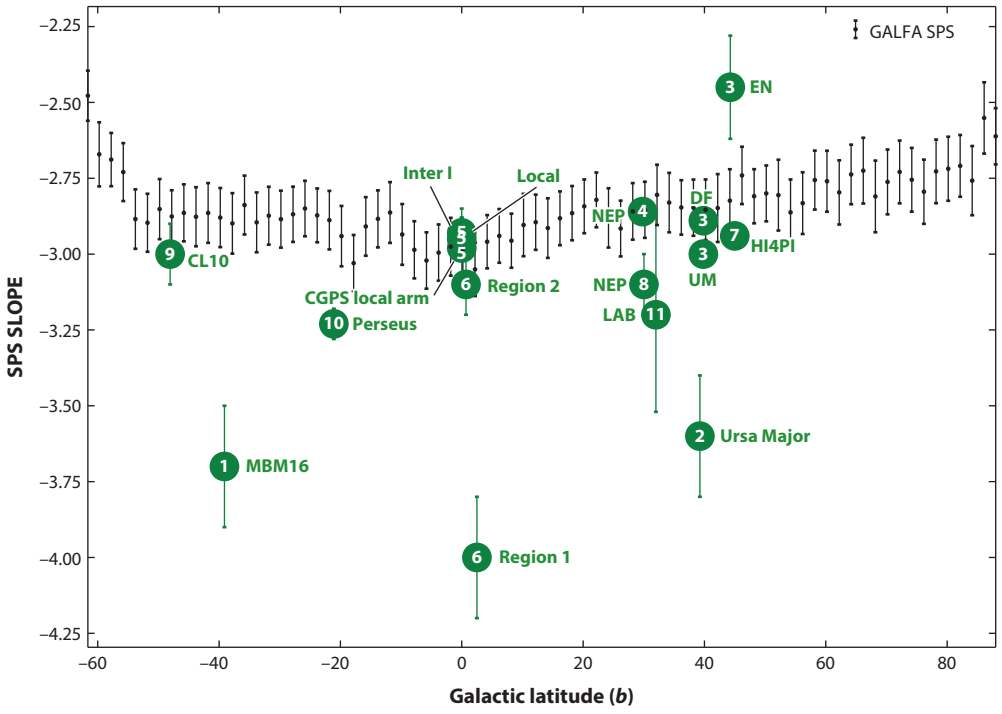


**Figure 9**

The spatial power spectrum (SPS) slope obtained for different HI regions as a function of Galactic latitude. All data points were derived from the HI column density images integrated over a certain range of velocities, focusing mostly on the low-velocity HI. Black data points are from A.K. Mittal, B.L. Babler & S. Stanimirović (manuscript in preparation). Green-dot numbers show data points from the following: 1, Pingel et al. (2013); 2, Miville-Deschênes et al. (2003); 3, Blagrave et al. (2017); 4, Martin et al. (2015); 5, Khalil et al. (2006); 6, Dickey et al. (2001); 7, Kalberla & Haud (2019); 8, Marchal & Miville-Deschênes (2021); 9, Chepurnov et al. (2010); 10, Pingel et al. (2018); 11, Choudhuri & Roy (2019).

It is interesting to see that the HI SPS slope appears relatively uniform across large spatial areas and is consistently only slightly shallower at high Galactic latitudes. The GALFA-HI survey samples the range of HI column densities from $\sim 10^{20}$ to $\sim 10^{22}$ cm$^{-2}$, yet the SPS slope remains largely around −2.8 for $|b| < 50$ deg. This could be due to the dominance of large-scale turbulent driving, on Galaxy- or kiloparsec-wide spatial scales, possibly caused by a combination of Galactic rotation, gravitational instabilities, infall onto the Galaxy, and even energy injection from large supershells (Wada et al. 2002, Bournaud et al. 2010, Krumholz & Burkhart 2016). Numerical simulations by Yoo & Cho (2014) have shown that the turbulent energy spectrum is very sensitive to large-scale driving. Unless the energy injection rates on small scales are much higher than on large scales, large-scale driving will always dominate. Therefore, even in the presence of significant stellar feedback in the Galactic Plane, large-scale turbulent driving might be the dominant mechanism. The finding of a relatively uniform SPS slope for the Milky Way resembles the situation with HI in the Small Magellanic Cloud, where Szotkowski et al. (2019) found a very uniform SPS slope across the entire galaxy.

Hennebelle & Falgarone (2012) showed that the kinetic energy transfer rate measured for the population of molecular clouds traced by $^{12}$CO did not vary with spatial scale ranging from ∼0.01 to ∼100 pc. They interpret this result as suggesting that molecular clouds are part of the same turbulent cascade as HI. From this point of view, the relatively uniform HI SPS slope may not

be very surprising—if molecular clouds of varying levels of star formation and stellar feedback sources do not show significant changes of their internal turbulent properties, the HI of the Milky Way may also not be strongly affected by small-scale turbulent driving.

In summary, while interpretation of the HI SPS remains complicated, some trends have begun to emerge from analyses of large surveys with consistent methodologies. Moving forward, it will be essential to develop a consistent and uniform approach for handling data, as well as more sophisticated methods for disentangling geometry, phase, and turbulent mode effects.

## 6.4. Three-Dimensional Distribution

Because of the nature of the large scales involved, our overall understanding of the 3D distribution of the Milky Way in HI has not changed much since the excellent review by Kalberla & Kerp (2009). These authors carefully explored the radial distribution, the warp, and the scale height of the warm disk. Key characteristics included an asymmetric warp beyond $R \approx 9$ kpc and a rapidly flaring disk beyond around $R > 18$ kpc.

**6.4.1. Radial distribution.** Like most HI-rich galaxies, the Milky Way has an extended HI disk. What is the true extent of the HI disk, and what form does it take? It is difficult to associate distances to HI emission in the outer Milky Way because observational methods are generally limited to kinematic distances. Assuming a mostly flat rotation curve, Kalberla & Dedes (2008) found that the HI disk extends beyond $R \sim 30$ kpc but that the HI surface density there is low: $N_{\rm H} \sim 1.5 \times 10^{19}$ cm$^{-2}$ or 0.1 $M_\odot$ pc$^{-2}$. At even larger galactocentric radii, the disk likely extends as far as 60 kpc but with a very high velocity dispersion ($\sigma_{\rm v} = 74$ km s$^{-1}$), which cannot be thermal and therefore must suggest a clumpy distribution with a high cloud-to-cloud velocity dispersion. A large radial extent to the HI disk has also been observed in other galaxies. For example, NGC 2997 (Pisano 2014) shows clumps of HI up to 60 kpc.

The tail end of the HI radial distribution, however, is at odds with previous theoretical estimates of the column density cutoff due to ionization from the CMB (e.g., Dove & Shull 1994, Maloney 1993), suggesting that the HI column density should drop precipitously after $R \sim 35$ kpc. Bland-Hawthorn et al. (2017) revisited the extended HI disk models that included the effects of nonuniform gas distribution or reducing the scale height. They showed that if the HI distribution were compressed into a narrower scale height, which would increase the mean volume density by a factor of 100 to $n_{\rm H} \sim 10$ cm$^{-3}$, the disk could survive as HI with $N_{\rm H} > 10^{18}$ cm$^{-2}$ to $R > 55$ kpc. But the radial extent of the disk is strongly dependent on the assumed mean volume density; reducing to $n_{\rm H} \sim 1$ cm$^{-3}$ decreases the disk radius at the same sensitivity limit to $R \sim 45$ kpc.

Explaining the Milky Way's apparently large, low-column, radial extent relies on both increasing the mean volume density and explaining the high velocity dispersion. The latter might be attributed to the discrete extended HI line wings like those observed by Kang & Koo (2007) and tentatively associated with old supernova remnants. The evidence for the large volume density predicted by Bland-Hawthorn et al. (2017) is less clear. Certainly, we know from Strasser et al. (2007) and Dickey et al. (2009) that dense material exists at radii $15 < R < 25$ kpc with estimated number densities of $n_{\rm H} \approx 0.7$–$2.4$ cm$^{-3}$.

Note that there is some direct evidence that the HI extends at least as far as $R = 23$ kpc. This evidence comes from the interaction between the Magellanic Leading Arm and the Galactic disk (McClure-Griffiths et al. 2004, Price-Whelan et al. 2019) at $R = 23$ kpc, which resulted in an orphan star cluster that is associated with the Magellanic Leading Arm and formed from the interaction with the disk. Nidever et al. (2019) used the full 3D velocity vector and star cluster's orbit to predict the gas density of the disk through which the cluster passed. This interesting

example provides an unusual method to estimate the density of the HI disk at the midplane at $R = 20$ kpc: $n_H = 6.0 \times 10^{-2}$ cm$^{-3}$.

The CNM and WNM have different spatial extents. Unlike those of the warm gas, the scale height and extent of the CNM disk have not been well characterized. For the most part, this has been an observational limitation; HI emission is dominated by warm gas, and the only places where the profiles are simple enough to allow CNM–WNM decomposition are at high latitudes and dominated by the local gas. Nonetheless, the sheer number of HI absorption measurements enabled by the Galactic Plane surveys (CGPS, Taylor et al. 2003; VGPS, Stil et al. 2006; SGPS, McClure-Griffiths et al. 2005; THOR, Wang et al. 2020b) indicates the extent of the cold disk.

The cold HI disk extends to at least 25 kpc and shows a distinct pattern in longitude–velocity space that nominally traces the spiral arm distribution (Strasser et al. 2007). As discussed above in Section 5.2, Dickey et al. (2009) showed that the CNM fraction remained mostly flat with Galactic radius out to at least 20 kpc, with the assumption that the average temperature of the cold component does not change. Dickey et al. (2022) recently revisited that result by stacking 175 HI absorption spectra toward extragalactic sources from the new Galactic Australian SKA Pathfinder (GASKAP) Pilot Survey. They found that the 2009 result stands, with a constant CNM fraction out to $R \sim 40$ kpc. These results are somewhat surprising; the outer Galaxy environment has a much lower metallicity (possibly less than one-tenth the Solar Circle gas-phase O/H abundance; Wenger et al. 2019), and the balance of heating and cooling is likely quite different.

**6.4.2. Scale height.** The scale height of the HI emission layer and its variations with galactocentric radius exterior to the Solar Circle have been well measured by Kalberla & Dedes (2008) and summarized in a review by Kalberla & Kerp (2009). Kalberla & Kerp (2009) described the radial dependence of the FWHM of the emission layer between $R = 5$ kpc and $R = 35$ kpc as $f = f_0 e^{(R-R_0)/R_0}$, where $f_0 = 300$ pc and $R_0 = 9.8$ kpc. Interior to the Solar Circle, in the range $4 \lesssim R \lesssim 8$ kpc, the density, $n(z)$, of the HI disk in the inner Galaxy has long been characterized by a dual Gaussian with FWHM values of 212 pc and 530 pc, with an additional low-density exponential tail (Lockman et al. 1986, Dickey & Lockman 1990, Savage & Wakker 2009). The full distribution has an FWHM of 430 pc, but Lockman (1984) observed that inside approximately $R = 2$ kpc, the scale height appeared to decrease. This observation was confirmed in detail by Lockman & McClure-Griffiths (2016), who showed that from $R \approx 2.1$ kpc on the negative-longitude side of the Galactic Center to $R \approx 2.4$ kpc on the positive-longitude side the large scale height layer is missing and the disk is very well fitted by a single Gaussian with FWHM $\sim 125$ pc. This diminished disk accompanies a dramatic reduction in the HI surface density in the inner 2.5 kpc of the Galaxy. At $R = 3.5$–$3.75$ kpc, the surface density is $\Sigma_{HI} = 3.4$ M$_\odot$ pc$^{-2}$, dropping to $\Sigma_{HI} = 0.4$ M$_\odot$ pc$^{-2}$ in the annulus from 1.5 kpc to 1.75 kpc. The cause of the significant drop in HI surface density is not clear; possible causes are related to the conversion of HI to molecular material, evacuation due to Galactic Center activity, or simply an observational effect of noncircular orbits (Lockman & McClure-Griffiths 2016).

The scale height of the HI emission disk may also vary in the outer Galaxy. Working from a flat rotation curve, Levine et al. (2006) transformed the brightness temperature distribution of HI emission, $T(l, b, v)$, to an estimated number density distribution, $n(R, z, \phi)$, and found variations in the scale height of 15–20%, which correlated with variations in the HI gas surface density $\Sigma_{HI}$ of 30–50%. Using a similar technique, but fitting for the rotation curve as well, Kalberla et al. (2007) found the same general trends. The conclusions from these studies are that the gas disk is thinner where the surface density is higher and that these variations correlate with spiral structure. Note, however, that these conclusions are based on nearly flat, azimuthally smooth rotation curves. We know that dense spiral arms can drive deviations of up to 10% from a flat rotation curve (Burton

1971, McClure-Griffiths & Dickey 2016, Peek et al. 2022), which in turn can drive systematic variations in distance-dependent properties. The suggestion that variations in the HI scale height correlate with spiral arms should therefore be viewed with some caution.

While the distribution of the HI emission layer has been well characterized across the Galaxy, the distribution of the cold HI disk has been much more difficult to constrain. Focusing on the Solar Neighborhood, Crovisier (1978) pioneered a technique to ascertain the scale height of the cold HI disk at the Solar Circle from observations of HI in absorption. By comparing the radial velocities in a catalog of absorbing HI clouds at $|b| > 10$ deg (isolating only the local clouds) with those expected for clouds in a differentially rotating disk, Crovisier (1978), and later Belfort & Crovisier (1984), estimated the mean distance of local HI clouds from the plane to be $\langle|z|\rangle \approx$ 100 pc. Both Crovisier (1978) and Belfort & Crovisier (1984) found that $\langle|z|\rangle$ increased at higher latitudes ($|b| \gtrsim 20$ deg), which they interpreted as a result of the low abundance of HI clouds very near the Sun. For a Gaussian distribution, $\langle|z|\rangle = 100$ pc corresponds to an FWHM of almost 300 pc.

The irregular aerial sampling of HI absorption through the low Galactic latitudes, which are most useful for probing the scale height of the cold disk, has limited our understanding of the CNM disk structure away from the Solar Neighborhood. Dickey et al. (2009) used the Galactic Plane surveys to produce a projection of HI opacity as a function $R$ and $\phi$ outside the Solar Circle. Recently, measurements by Dickey et al. (2022) of HI absorption toward 175 extragalactic continuum sources in the GASKAP Pilot region provided the first indications of the scale height of the CNM disk in several regions away from the Solar Circle. Dickey et al. stacked HI absorption spectra from the region 338 deg $\leq l \leq$ 342 deg, focusing on regions exterior to the Solar Circle and in the inner galaxy at the subcentral point where the line of sight is tangent to a circular orbit around the Galactic Center and the HI reaches its terminal velocity (e.g., McClure-Griffiths & Dickey 2016). These measurements, together with Solar Neighborhood measurements (Crovisier 1981, Belfort & Crovisier 1984), are starting to give a clear picture of variations in the height of the cold HI disk with galactocentric radius.

**Figure 10** compares the $z$ structure of the emission and absorption disks in the inner and outer Galaxy. This figure compiles the data from Dickey et al. (2022), comparing the averaged HI absorption $\langle 1-\exp(-\tau)\rangle\ \Delta v$ with the averaged HI emission $\langle T_b\rangle$ as a function of latitude in a region in the inner ($R \sim 2.7$ kpc) and outer ($R \sim 12.8$ kpc) Galaxy. The inner Galaxy region shows the absorption and emission only at the terminal velocity, $-145$ km s$^{-1} < v_{\rm LSR} < -125$ km s$^{-1}$, where the distance is geometrically defined at $d \sim 7.8$ kpc for $R_\odot = 8.3$ kpc. The outer Galaxy region shows absorption and emission between 15 km s$^{-1} < v_{\rm LSR} < 35$ km s$^{-1}$, where, for a flat rotation curve, $d \approx 20$ kpc and $R \sim 12.5$ kpc. Fitting to the normalized $z$ distributions, we find that the FWHM of the absorption disk is 185 pc at $R \sim 2.8$ kpc and 490 pc at $R \sim 12.5$ kpc, while the inner and outer Galaxy emission FWHM values are 245 pc and 710 pc, respectively. The fits are consistent with those of Dickey et al. (2022), yet we also confirm the classic view that for the inner Galaxy the emission is better fit with two Gaussians of FWHM 110 and 340 pc, while the low resolution of HI4PI limits the outer Galaxy fit to a single Gaussian component. The key conclusions from the comparison are that (*a*) the absorption disk is narrower than the emission disk at all Galactic radii and (*b*) the absorption and emission disks are narrower in the inner Galaxy than in the outer Galaxy. When these data are combined with the data from Crovisier (1981), a picture develops of the cold HI disk increasing in thickness from an FWHM of ∼185 pc at $R \sim$ 2.8 kpc to 300 pc around the Sun to ∼490 pc at $R \sim 12.5$ kpc (**Figure 11**). These conclusions are not necessarily surprising, given the higher pressure in the inner Galaxy, but they suggest that the cold HI gas disk more closely matches the $H_2$ disk than the warm HI.

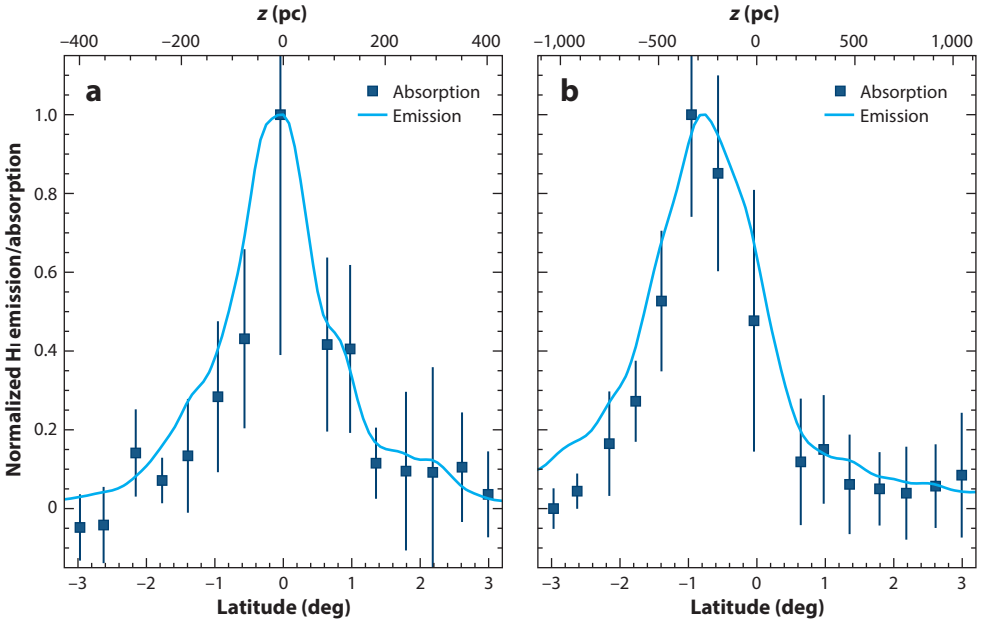


**Figure 10**

Normalized distributions of average fractional absorption, $\langle 1 - e^{-\tau} \rangle$, and average emission, $\langle T_b \rangle$, versus Galactic latitude between $l = 339$ deg and $l = 342$ deg for velocities (*a*) close to the inner Galaxy tangent point at $R \sim 2.8$ kpc and (*b*) in the outer Galaxy at $R \sim 12.5$ kpc. The upper axis in $z$ is for an assumed distance of $d = 7.3$ kpc and $d = 20$ kpc for the tangent point, and an assumed flat rotation curve with $R_\odot = 8.31$ kpc and $\Theta_0 = 240$ km s$^{-1}$ (Reid et al. 2019). Emission data points were derived from GASS (McClure-Griffiths et al. 2009, Kalberla et al. 2010). Absorption data points were adapted with permission from Dickey et al. (2022).

Ideally, analyses like those by Dickey et al. (2009, 2022) will be extended across the Galactic disk to help us realize an azimuthally resolved view of the disk scale height. If noncircular motions can be accounted for with future stellar-derived mass models for the Milky Way, we might hope to incorporate them so as to overcome problems related to the rotation curve.

## 7. FUTURE PROSPECTS FOR HI IN THE MILKY WAY

The field of HI in the Milky Way is once again poised for an observational revolution. The new SKA Pathfinders, ASKAP and MeerKAT, are providing highly sensitive interferometric data over wide fields, helping to bridge the gap between the limited-area, low-sensitivity interferometric surveys with approximately arcminute resolution and the large-area, high-sensitivity single-dish surveys with 3–16 arcmin resolution. MeerKAT has a 1 deg field of view with outstanding surface brightness sensitivity at subarcminute angular resolution. With its surface brightness sensitivity, MeerKAT will make excellent contributions to highly sensitive imaging over areas of tens of square degrees. We envision that MeerKAT will lead the way with deep, 10 arcsec imaging of high-latitude HI, with applications in phase decomposition of HI emission and studies of turbulence.

ASKAP uses phased-array technology to extend its field of view to ∼25 deg$^{-2}$, with a surface brightness sensitivity at 30 arcsec that is similar to those of previous interferometric HI surveys but 300 times faster (Hotan et al. 2021). The GASKAP-HI survey specifically targets HI in the Milky Way at high angular (∼30 arcsec) and spectral (∼0.4 km s$^{-1}$) resolution, with an order-of-magnitude improvement in sensitivity and angular resolution on the Galactic Plane,

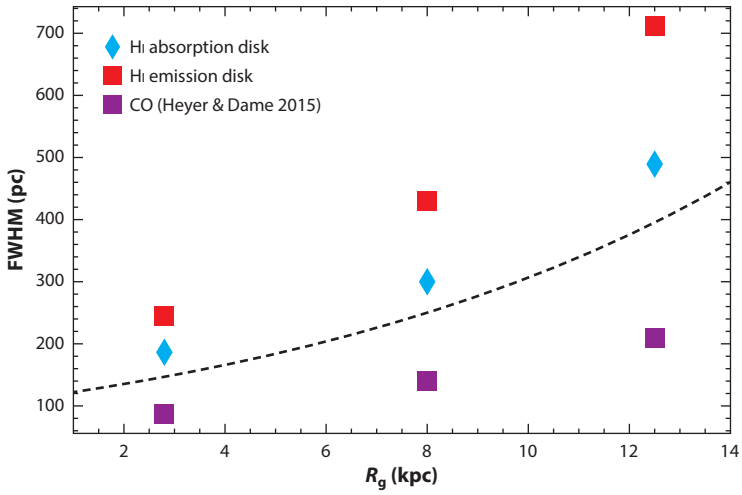


**Figure 11**

Scale-height comparison of cold and warm HI with a CO disk as a function of Galactocentric radius. Blue points represent the full width at half-maximum (FWHM) of the absorption disk, red points represent the FWHM of the emission disk, and purple points represent the FWHM of the CO from Heyer & Dame (2015). The dashed line represents the Kalberla & Kerp (2009) fit for $n(z)$, based on the assumption of hydrostatic equilibrium. Absorption data are from Crovisier (1981) and Dickey et al. (2022). Emission FWHM values were calculated from Gaussian fits to HI4PI data (Ben Bekhti et al. 2016).

Galactic Center, and a large swathe of high-latitude sky covering the Magellanic Clouds and Stream plus the Milky Way foreground. GASKAP-HI will jointly deliver HI emission images and catalogs of HI absorption. These data will be outstanding for joint studies of the CNM and WNM distribution with galactocentric radius and in $z$ height.

HI absorption surveys at high Galactic latitudes have been slow to carry out and almost exclusively targeted. For example, the MACH survey measured HI absorption in the direction of only 42 background sources in 50 h of observation with the VLA to trace the latitude dependence of absorption properties. The GASKAP-HI high-latitude survey will obtain ∼150 absorption spectra with a quality similar to MACH in every 25 deg$^2$ field after 30 h of integration. In the Galactic foreground of the Magellanic Stream, GASKAP-HI should yield more than 7,000 new HI absorption measurements over a range of Galactic latitudes. The spatial sampling of this "HI absorption grid" will help trace variations in spin temperature and column density over scales of a parsec or less.

The next major advance in HI studies of the Milky Way will come when the spatial sampling of an all-sky irregular grid of HI absorption finally reaches the effective angular resolution that we currently have with HI4PI in emission. The full SKA, when it becomes operational around 2028, will extend Milky Way HI studies further in both emission and absorption. Together, the pathfinders and ultimately the SKA will be able to provide a catalog several orders of magnitude larger than the BIGHICAT, with values of optical depth, spin temperature, and column density determined from a dense grid of absorption measurements. That will finally allow us to realize the goal of having all (Southern-)sky cubes of the CNM with an effective resolution of $\lesssim$0.25 deg.

Two other telescopes that will enormously improve the sensitivity of HI surveys are the Five-Hundred-Meter Aperture Spherical Telescope (FAST) for HI emission and the next-generation Very Large Array (ngVLA) for HI absorption. With its 500 m collecting area, FAST can reach brightness temperature sensitivity limits better than any other telescope in the world at an angular resolution of a few arcminutes. ngVLA, if designed to specification, will be superb for measuring

HI absorption to deduce the properties of the WNM. ngVLA should produce absorption spectra with ~60 times lower noise for a given observation time than 21-SPONGE, which is the most sensitive comprehensive survey of HI absorption. If the spectral baselines are stable, ngVLA should produce observations at $\sigma_\tau < 10^{-5}$ toward bright (~1–10 Jy) sources with minimal telescope time.

As we move into the realm of big data for HI, it will no longer be possible to look at each cube and fit each spectrum by hand. It will be essential to employ new techniques to extract physical properties from the data and to characterize the morphological interpretation of multidimensional data. Some of these new techniques have recently been tested and applied to new surveys (e.g., Gausspy, Lindner et al. 2015; ROHSA, Marchal et al. 2019; AstroHOG, Soler et al. 2019; RHT, Clark et al. 2015; CNN, Murray et al. 2021). New tools and techniques to analyze the spectrally and spatially complex HI datasets will be essential to further our understanding of HI in the Milky Way. Applying these techniques to synthetic observations of simulations will help us infer astrophysical quantities from observational HI data.

## 7.1. Future Complementary Data

New HI data will be complemented by other datasets capable of tracing the dust, molecular gas, and magnetic field structure of the ISM with better resolution in all dimensions. We are already starting to see the power of linking HI datasets with 3D dust distribution within a few hundred parsecs of the Sun (e.g., Green et al. 2019, Lallement et al. 2019, Leike et al. 2020, Vergely et al. 2022). For example, Panopoulou & Lenz (2020) used the association with dust to show that there are two to three kinematically distinct HI components along most high Galactic latitude lines of sight. Tchernyshyov & Peek (2017) and Tchernyshyov et al. (2018) used the 3D dust distribution along with HI data to obtain 4D (three spatial plus one velocity) information about the gas distribution. While these dust maps are currently limited to local gas, future infrared surveys with the *Nancy Grace Roman Space Telescope* could be used to extend the 3D dust distribution within the Galactic Plane to much further distances. Associating HI with dust to derive distances and trace 4D HI information will open new opportunities to use HI for spiral structure, physical gas properties, and many other areas.

Essential to the interpretation of future observational data will be future simulations at subparsec resolution over the full disk of a galaxy to trace the microphysics visible through our new observational datasets. Simulations have a particular advantage in that they can turn on and off individual heating and cooling processes and introduce different feedback channels. By comparing the simulated mass fractions across different phases with observations, we can gain insight into the importance of various feedback channels. From this point of view, a database of simulations made consistently while varying different input parameters would be very useful for future investigations. With thousands of HI absorption spectra to be provided by future surveys, we envision that both observations and simulations could start to focus on individual regions (e.g., Galactic Center versus outer regions, the HI warp, off-plane), instead of the entire Milky Way, to investigate the mass flow of HI across different phases and how it changes with local conditions.

## 7.2. Future Questions

Throughout the compilation of this review, we encountered countless questions for future research. It is impossible to describe them all here, but we have chosen to list below some of the biggest questions that we might reasonably hope to answer within the next decade through a savvy combination of multiwavelength observational and simulated datasets and new techniques.

1. New surveys of HI absorption will expand the number of HI absorption detections by a factor of more than 100 to answer questions about how the spin temperature changes with

location around the Galaxy, revealing what fraction of the observed HI is in the UNM and how this fraction varies with environment. These extensive databases of HI absorption should show how the HI excitation processes and the heating and cooling rates change with environment, e.g., within the star-forming disk versus the halo, and inner versus outer disk regions.

2. Projects combining stellar and dust distances to produce a complex model of the 3D structure of the Milky Way's ISM are underway. Coupling a 3D ISM model with HI spectra will help break some of the current distance–velocity degeneracies that trouble HI. In so doing, we hope to be able to answer the following questions: How do the HI properties correlate with large-scale Galactic structure? Are there opacity or scale-height variations with *R* and azimuth? Can HI be routinely linked to dust to provide 3D spatial information along with velocity information? The 3D dust and stellar distribution models will also help researchers create a 3D UV radiation field to understand how the HI properties change with local UV radiation field or column density.
3. By combining new high spatial and spectral resolution HI surveys with machine learning and other spectral decomposition techniques, future studies may be able to investigate the CNM and WNM separately everywhere in the Galaxy. We hope that combining fully decomposed atlases of the CNM and WNM with ever-improving statistical descriptors of morphology (e.g., Rayleigh statistics; Soler et al. 2020) will enable researchers to understand the differences in structure between the phases and whether magnetic fields are a dominant contributor to the structure of the HI in both the CNM and WMN or only in the CNM.
4. With the revolution of large-area, high-resolution HI observations, HI will remain a unique tracer for observationally determining the relative importance of various turbulent driving modes in diverse ISM environments. As numerical simulations become increasingly complex and move beyond prescribed turbulence driving to directly include various channels of stellar feedback, they will require the detailed understanding of these modes' effects on the surrounding ISM that will be gained from future statistical studies of HI.

Perhaps the most important question is: What lessons can we take from the Milky Way to help us understand other galaxies? Over the next 5 years, extragalactic HI surveys with JVLA, ASKAP, and MeerKAT will start to reveal nearby galaxies with the spatial resolution and number of HI absorption spectra that we have presented for the Milky Way in this review. Through a comparison of Milky Way HI with the properties of HI measured in nearby galaxies, we will start to probe how the HI phases respond to metallicity and vastly different UV radiation fields. This review begins by noting that it is only in the Milky Way that we can resolve the subparsec scales needed to understand the transition from the WNM to the CNM and its role as a throttle in star formation. It is not obvious that we understand the full details of that transition, but it is clear that the physics is rich and that, by extending detailed HI studies from the Milky Way to other galactic environments, we just might reach an answer.

## SUMMARY POINTS

1. The cold neutral medium (CNM) is ubiquitous in the Milky Way. The CNM temperature distribution peaks at 50–200 K and is broad, likely due to the sampling of both dense and diffuse environments. Some evidence exists that only colder and denser CNM goes

on to form $H_2$. The CNM temperature decreases with $A_V$: Higher-$A_V$ regions have a lower $T_s$, while lower-$A_V$ regions have a higher $T_s$.

2. The average CNM mass fraction in the Milky Way is ~40%. The CNM fraction increases with $A_V$ due to the increase of the mean density. Local density plays a strong role in constraining the CNM fraction and spin temperature. The morphology of the CNM, as observed in emission, is highly filamentary and is correlated with the orientation of the magnetic fields.
3. The unstable neutral medium (UNM) remains difficult to constrain observationally because it requires highly sensitive absorption measurements. The most robust estimate to date for the average UNM mass fraction is ~20%, in agreement with predictions from some recent numerical simulations. The morphology, spatial distribution, and other properties of the UNM remain open questions.
4. The warm neutral medium (WNM) peak of the HI temperature distribution remains observationally unconstrained from HI absorption observations due to its very low optical depth. The likely reason is that the WNM has a higher excitation temperature than what has been assumed over the last few decades. The spatial distribution of the WNM in relation to the CNM and UNM needs better constraints. The average WNM mass fraction is ~40%; even the densest ISM regions have some WNM. Shells and superbubbles are important for setting the HI emission morphology and create HI structures as broken remnants of shells and supershells are driven away from the disk.
5. The interpretation of the spatial power spectrum (SPS) of HI emission depends on many effects. Large areas of the Milky Way appear to have a relatively uniform SPS slope.
6. The cold disk of the Milky Way extends to at least three times the solar radius. Throughout the disk, the CNM has a scale height that is intermediate between that of the WNM and the molecular gas.

## DISCLOSURE STATEMENT

The authors are not aware of any affiliations, memberships, funding, or financial holdings that might be perceived as affecting the objectivity of this review.

## ACKNOWLEDGMENTS

We have benefited enormously from conversations with S. Bialy, J.M. Dickey, M. Gong, P. Hennebelle, A.S. Hill, C.-G. Kim, A. Marchal, M.-A. Miville-Deschênes, C. Murray, and H. Nguyen. We are very grateful to Eve Ostriker for many suggestions that improved an early version of this review. We are grateful to Amit Mittal for providing **Figure 9**. The authors acknowledge the Interstellar Institute's program "With Two Eyes" and the Paris-Saclay University's Institut Pascal for hosting discussions that nourished the development of the ideas behind this article. The authors are grateful to D. McConnell for significant comments on drafts of this review. N.M.M.-G. acknowledges funding support through an Australian Research Council Laureate Fellowship (project number FL210100039) funded by the Australian Government. S.S. and D.R.R. acknowledge support provided by the University of Wisconsin–Madison Office of the Vice Chancellor for Research and Graduate Education with funding from the Wisconsin Alumni Research Foundation. The writing of this review was supported by National Science

Foundation award AST-2108370 and by the National Aeronautics and Space Administration under grant 4200766703.

## LITERATURE CITED

Ade PAR, Aghanim N, Arnaud M, et al. (PLANCK Collab.). 2011. *Astron. Astrophys.* 536:A19
Audit E, Hennebelle P. 2005. *Astron. Astrophys.* 433:1–13
Baker PL, Burton WB. 1979. *Astron. Astrophys. Suppl. Ser.* 35:129–52
Beaumont CN, Offner SSR, Shetty R, Glover SCO, Goodman AA. 2013. *Ap. J.* 777(2):173
Begum A, Stanimirović S, Goss WM, et al. 2010. *Ap. J.* 725(2):1779–85
Belfort P, Crovisier J. 1984. *Astron. Astrophys.* 136:368–70
Ben Bekhti N, Flöer L, Keller R, et al. (HI4PI Collab.). 2016. *Astron. Astrophys.* 594:A116
Beuther H, Bihr S, Rugel M, et al. 2016. *Astron. Astrophys.* 595:A32
Beuther H, Wang Y, Soler J, et al. 2020. *Astron. Astrophys.* 638:A44
Bialy S. 2020. *Ap. J.* 903(1):62
Bialy S, Sternberg A. 2019. *Ap. J.* 881(2):160
Bihr S, Beuther H, Ott J, et al. 2015. *Astron. Astrophys.* 580:A112
Blagrave K, Martin PG, Joncas G, et al. 2017. *Ap. J.* 834(2):126
Bland-Hawthorn J, Maloney PR, Stephens A, Zovaro A, Popping A. 2017. *Ap. J.* 849(1):51
Bournaud F, Elmegreen BG, Teyssier R, Block DL, Puerari I. 2010. *MNRAS* 409(3):1088–99
Bracco A, Jelić V, Marchal A, et al. 2020. *Astron. Astrophys.* 644:L3
Braun R, Walterbos RAM. 1992. *Ap. J.* 386:120–38
Burton WB. 1971. *Astron. Astrophys.* 10:76–96
Burton WB. 1988. In *Galactic and Extragalactic Radio Astronomy*, ed. GL Verschuur, KI Kellermann, pp. 295–358. Berlin: Springer. 2nd ed.
Campbell JL, Clark SE, Gaensler BM, et al. 2022. *Ap. J.* 927(1):49
Carilli CL, Dwarakanath KS, Goss WM. 1998. *Ap. J. Lett.* 502(1):L79–83
Carilli CL, Walter F. 2013. *Annu. Rev. Astron. Astrophys.* 51:105–61
Chengalur JN, Kanekar N, Roy N. 2013. *MNRAS* 432(4):3074–79
Chepurnov A, Lazarian A, Stanimirović S, Heiles C, Peek JEG. 2010. *Ap. J.* 714:1398–406
Choudhuri S, Roy N. 2019. *MNRAS* 483(3):3437–43
Clark BG. 1965. *Ap. J.* 142:1398–422
Clark PC, Glover SCO, Klessen RS, Bonnell IA. 2012. *MNRAS* 424(4):2599–613
Clark SE, Hensley BS. 2019. *Ap. J.* 887(2):136
Clark SE, Hill JC, Peek JEG, Putman ME, Babler BL. 2015. *Phys. Rev. Lett.* 115:241302
Clark SE, Peek JEG, Miville-Deschênes MA. 2019. *Ap. J.* 874(2):171
Clark SE, Peek JEG, Putman ME. 2014. *Ap. J.* 789(1):82
Cortese L, Catinella B, Smith R. 2021. *Publ. Astron. Soc. Aust.* 38:e035
Cox DP. 2005. *Annu. Rev. Astron. Astrophys.* 43:337–85
Cox DP, Smith BW. 1974. *Ap. J. Lett.* 189:L105–8
Crovisier J. 1978. *Astron. Astrophys.* 70:43–50
Crovisier J. 1981. *Astron. Astrophys.* 94:162–74
Crovisier J, Dickey JM. 1983. *Astron. Astrophys.* 122:282–96
Crovisier J, Kazes I, Aubry D. 1978. *Astron. Astrophys. Suppl. Ser.* 32:205–82
Crutcher RM. 1999. *Ap. J.* 520:706–13
Dawson JR, McClure-Griffiths NM, Kawamura A, et al. 2011. *Ap. J.* 728:127
Dawson JR, Mizuno N, Ohnishi T, McClure-Griffiths NM, Fukui Y. 2008. *MNRAS* 387(1):31–44
Deguchi S, Watson WD. 1985. *Ap. J.* 290:578–86
Dénes H, McClure-Griffiths NM, Dickey JM, Dawson JR, Murray CE. 2018. *MNRAS* 479(2):1465–90
Dickey JM, Benson JM. 1982. *Astron. J.* 87:278–305
Dickey JM, Dempsey JM, Pingel NM, et al. 2022. *Ap. J.* 926(2):186
Dickey JM, Lockman FJ. 1990. *Annu. Rev. Astron. Astrophys.* 28:215–61

Dickey JM, McClure-Griffiths NM, Gaensler BM, Green AJ. 2003. *Ap. J.* 585:801–22
Dickey JM, McClure-Griffiths NM, Stanimirović S, Gaensler BM, Green AJ. 2001. *Ap. J.* 561:264–71
Dickey JM, Salpeter EE, Terzian Y. 1977. *Ap. J. Lett.* 211:L77–81
Dickey JM, Salpeter EE, Terzian Y. 1978. *Ap. J. Suppl.* 36:77–114
Dickey JM, Strasser S, Gaensler BM, et al. 2009. *Ap. J.* 693:1250–60
Dobbs CL, Pringle JE, Burkert A. 2012. *MNRAS* 425:2157–68
D'Onghia E, Fox AJ. 2016. *Annu. Rev. Astron. Astrophys.* 54:363–400
Dove JB, Shull JM. 1994. *Ap. J.* 423:196–206
Dwarakanath KS, Carilli CL, Goss WM. 2002. *Ap. J.* 567:940–46
Ehlerová S, Palous J. 2005. *Astron. Astrophys.* 437:101–12
Ehlerová S, Palouš J. 2013. *Astron. Astrophys.* 550:A23
Ekers RD, Rots AH. 1979. In *Image Formation from Coherence Functions in Astronomy*, ed. C van Schooneveld, D Reidel, pp. 61–63. Berlin: Springer
Elmegreen BG, Elmegreen DM, Leitner SN. 2003. *Ap. J.* 590(1):271–83
Elmegreen BG, Scalo J. 2004. *Annu. Rev. Astron. Astrophys.* 42:211–73
Ewen HI, Purcell EM. 1951. *Nature* 168:356–58
Field GB. 1958. *Proc. IRE* 46:240–50
Field GB, Goldsmith DW, Habing HJ. 1969. *Ap. J. Lett.* 155:L149–54
Ford HA, Lockman FJ, McClure-Griffiths NM. 2010. *Ap. J.* 722:367–79
Ford HA, McClure-Griffiths NM, Lockman FJ, et al. 2008. *Ap. J.* 688:290–305
Fukui Y, Okamoto R, Kaji R, et al. 2014. *Ap. J.* 796:59
Fukui Y, Onishi T, Abe R, et al. 1999. *Publ. Astron. Soc. Jpn.* 51(6):751–64
Fukui Y, Torii K, Onishi T, et al. 2015. *Ap. J.* 798(1):6
Gibson SJ, Taylor AR, Higgs LA, Brunt CM, Dewdney PE. 2005a. *Ap. J.* 626:195–213
Gibson SJ, Taylor AR, Higgs LA, Brunt CM, Dewdney PE. 2005b. *Ap. J.* 626:214–32
Gibson SJ, Taylor AR, Higgs LA, Dewdney PE. 2000. *Ap. J.* 540:851–62
Glover SCO, Clark PC. 2012. *MNRAS* 421(1):9–19
Glover SCO, Federrath C, Mac Low MM, Klessen RS. 2010. *MNRAS* 404(1):2–29
Goldbaum NJ, Krumholz MR, Matzner CD, McKee CF. 2011. *Ap. J.* 738(1):101
Gong M, Ostriker EC, Wolfire MG. 2017. *Ap. J.* 843(1):38
González-Casanova DF, Lazarian A. 2017. *Ap. J.* 835(1):41
Green DA. 1993. *MNRAS* 262:327–42
Green GM, Schlafly E, Zucker C, Speagle JS, Finkbeiner D. 2019. *Ap. J.* 887(1):93
Grenier IA, Casandjian JM, Terrier R. 2005. *Science* 307:1292–95
Grisdale K, Agertz O, Renaud F, Romeo AB. 2018. *MNRAS* 479(3):3167–80
Grisdale K, Agertz O, Romeo AB, Renaud F, Read JI. 2017. *MNRAS* 466(1):1093–110
Hagen JP, Lilley AE, McClain EF. 1955. *Ap. J.* 122:361–75
Haud U, Kalberla PMW. 2007. *Astron. Astrophys.* 466:555–64
Haworth TJ, Glover SCO, Koepferl CM, Bisbas TG, Dale JE. 2018. *New Astron. Rev.* 82:1–58
Hayashi K, Okamoto R, Yamamoto H, et al. 2019. *Ap. J.* 878(2):131
Heeschen DS. 1955. *Ap. J.* 121:569–84
Heiles C. 1979. *Ap. J.* 229:533–37
Heiles C. 1984. *Ap. J. Suppl.* 55:585–95
Heiles C. 1989. *Ap. J.* 336:808–21
Heiles C. 1997. *Ap. J.* 481:193–204
Heiles C. 1998. *Ap. J.* 498:689–703
Heiles C. 2000. *Astron. J.* 119:923–27
Heiles C, Troland TH. 2003a. *Ap. J. Suppl.* 145:329–54
Heiles C, Troland TH. 2003b. *Ap. J.* 586:1067–93
Heiles C, Troland TH. 2004. *Ap. J. Suppl.* 151:271–97
Heiles C, Troland TH. 2005. *Ap. J.* 624:773–93
Hennebelle P, Audit E. 2007. *Astron. Astrophys.* 465:431–43

Hennebelle P, Falgarone E. 2012. *Astron. Astrophys. Rev.* 20:55
Hennebelle P, Inutsuka S-i. 2006. *Ap. J.* 647(1):404–11
Heyer M, Dame TM. 2015. *Annu. Rev. Astron. Astrophys.* 53:583–629
Hill AS, Mac Low MM, Gatto A, Ibáñez-Meja JC. 2018. *Ap. J.* 862(1):55
Hopkins PF, Grudić MY, Wetzel A, et al. 2020. *MNRAS* 491(3):3702–29
Hopkins PF, Quataert E, Murray N. 2012. *MNRAS* 421(4):3522–37
Hopkins PF, Wetzel A, Kereš D, et al. 2018. *MNRAS* 477(2):1578–603
Hotan AW, Bunton JD, Chippendale AP, et al. 2021. *Publ. Astron. Soc. Aust.* 38:e009
Hu EM. 1981. *Ap. J.* 248:119–27
Hu Y, Lazarian A, Xu S. 2021. arXiv:2104.02842 [astro-ph.GA]
Hughes MP, Thompson AR, Colvin RS. 1971. *Ap. J. Suppl.* 23:323–70
Iffrig O, Hennebelle P. 2017. *Astron. Astrophys.* 604:A70
Iwasaki K, Inutsuka S-i. 2014. *Ap. J.* 784(2):115
Kalberla PMW, Burton WB, Hartmann D, et al. 2005. *Astron. Astrophys.* 440:775–82
Kalberla PMW, Dedes L. 2008. *Astron. Astrophys.* 487:951–63
Kalberla PMW, Dedes L, Kerp J, Haud U. 2007. *Astron. Astrophys.* 469:511–27
Kalberla PMW, Haud U. 2015. *Astron. Astrophys.* 578:A78
Kalberla PMW, Haud U. 2018. *Astron. Astrophys.* 619:A58
Kalberla PMW, Haud U. 2019. *Astron. Astrophys.* 627:A112
Kalberla PMW, Kerp J. 2009. *Annu. Rev. Astron. Astrophys.* 47:27–61
Kalberla PMW, Kerp J, Haud U. 2020. *Astron. Astrophys.* 639:A26
Kalberla PMW, Kerp J, Haud U. 2021. *Astron. Astrophys.* 654:A91
Kalberla PMW, Kerp J, Haud U, et al. 2016. *Ap. J.* 821(2):117
Kalberla PMW, McClure-Griffiths NM, Pisano DJ, et al. 2010. *Astron. Astrophys.* 521:17
Kanekar N, Braun R, Roy N. 2011. *Ap. J. Lett.* 737(2):L33
Kanekar N, Subrahmanyan R, Chengalur JN, Safouris V. 2003. *MNRAS* 346(4):L57–61
Kang Jh, Koo BC. 2007. *Ap. J. Suppl.* 173(1):85–103
Khalil A, Joncas G, Nekka F, Kestener P, Arneodo A. 2006. *Ap. J. Suppl.* 165(2):512–50
Kim C-G, Kim JG, Gong M, Ostriker EC. 2022. arXiv:2211.13293 [astro-ph.GA]
Kim C-G, Ostriker EC. 2017. *Ap. J.* 846(2):133
Kim C-G, Ostriker EC. 2018. *Ap. J.* 853(2):173
Kim C-G, Ostriker EC, Kim WT. 2013. *Ap. J.* 776:1
Kim C-G, Ostriker EC, Kim WT. 2014. *Ap. J.* 786:64
Kim JG, Kim WT. 2013. *Ap. J.* 779(1):48
Knapp GR. 1974. *Ap. J.* 79:527–54
Knapp GR, Verschuur GL. 1972. *Astron. J.* 77:717–25
Knee LBG, Brunt CM. 2001. *Nature* 412:308–10
Koch EW, Rosolowsky EW, Schruba A, et al. 2019. *MNRAS* 485(2):2324–42
Körtgen B, Pingel N, Killerby-Smith N. 2021. *MNRAS* 505(2):1972–86
Koyama H, Inutsuka S. 2000. *Ap. J.* 532:980–93
Koyama H, Inutsuka S. 2002. *Ap. J.* 564:L97–100
Kritsuk AG, Norman ML, Padoan P, Wagner R. 2007. *Ap. J.* 665:416–31
Krumholz MR, Burkhart B. 2016. *MNRAS* 458(2):1671–77
Krumholz MR, Leroy AK, McKee CF. 2011. *Ap. J.* 731:25
Krumholz MR, McKee CF, Tumlinson J. 2009. *Ap. J.* 693:216–35
Kulkarni SR, Fich M. 1985. *Ap. J.* 289:792–802
Kulkarni SR, Heiles C. 1987. In *Interstellar Processes*, ed. DJ Hollenbach, HA Thronson, pp. 87–122. Berlin: Springer
Kulkarni SR, Heiles C. 1988. In *Galactic and Extragalactic Radio Astronomy*, ed. GL Verschuur, KI Kellermann, pp. 95–153. Berlin: Springer. 2nd ed.
Lallement R, Babusiaux C, Vergely JL, et al. 2019. *Astron. Astrophys.* 625:A135
Lazareff B. 1975. *Astron. Astrophys.* 42:25–35

Lazarian A, Pogosyan D. 2000. *Ap. J.* 537:720–48
Lee MY, Stanimirovic S, Murray CE, Heiles C, Miller J. 2015. *Ap. J.* 809:56
Leike RH, Glatzle M, Enßlin TA. 2020. *Astron. Astrophys.* 639:A138
Leroy AK, Walter F, Brinks E, et al. 2008. *Astron. J.* 136:2782–845
Levine ES, Blitz L, Heiles C. 2006. *Ap. J.* 643:881–96
Li D, Goldsmith PF. 2003. *Ap. J.* 585:823–39
Li D, Goldsmith PF. 2012. *Ap. J.* 756:12
Lindner RR, Vera-Ciro C, Murray CE, et al. 2015. *Astron. J.* 149:138
Liszt H. 2001. *Astron. Astrophys.* 371:698–707
Liszt H, Gerin M, Grenier I. 2018. *Astron. Astrophys.* 617:A54
Lockman FJ. 1984. *Ap. J.* 283:90–97
Lockman FJ. 2002. *Ap. J. Lett.* 580:L47–50
Lockman FJ, Hobbs LM, Shull JM. 1986. *Ap. J.* 301:380–94
Lockman FJ, McClure-Griffiths NM. 2016. *Ap. J.* 826(2):215
Mac Low MM, Balsara DS, Kim J, de Avillez MA. 2005. *Ap. J.* 626(2):864–76
Maloney P. 1993. *Ap. J.* 414:41–56
Marchal A, Miville-Deschênes MA. 2021. *Ap. J.* 908(2):186
Marchal A, Miville-Deschênes MA, Orieux F, et al. 2019. *Astron. Astrophys.* 626:A101
Martin PG, Blagrave KPM, Lockman FJ, et al. 2015. *Ap. J.* 809(2):153
McClure-Griffiths NM, Dickey JM. 2016. *Ap. J.* 831(2):124
McClure-Griffiths NM, Dickey JM, Gaensler BM, Green AJ. 2001. *Ap. J.* 562:424–32
McClure-Griffiths NM, Dickey JM, Gaensler BM, Green AJ. 2002. *Ap. J.* 578:176–93
McClure-Griffiths NM, Dickey JM, Gaensler BM, Green AJ. 2003. *Ap. J.* 594:833–43
McClure-Griffiths NM, Dickey JM, Gaensler BM, Green AJ. 2004. *Ap. J. Lett.* 607:L127–30
McClure-Griffiths NM, Dickey JM, Gaensler BM, Green AJ, Haverkorn M. 2006. *Ap. J.* 652:1339–47
McClure-Griffiths NM, Dickey JM, Gaensler BM, Green AJ, Haverkorn M, Strasser S. 2005. *Ap. J. Suppl.* 158:178–87
McClure-Griffiths NM, Ford A, Pisano DJ, et al. 2006. *Ap. J.* 638:196–205
McClure-Griffiths NM, Pisano DJ, Calabretta MR, et al. 2009. *Ap. J. Suppl.* 181:398–412
McKee CF, Ostriker JP. 1977. *Ap. J.* 218:148–69
Mebold U, Düsterberg C, Dickey JM, Staveley-Smith L, Kalberla P. 1997. *Ap. J. Lett.* 490(1):L65–68
Mebold U, Winnberg A, Kalberla PMW, Goss WM. 1982. *Astron. Astrophys.* 115(2):223–41
Meyer DM, Lauroesch JT, Heiles C, Peek JEG, Engelhorn K. 2006. *Ap. J. Lett.* 650(1):L67–70
Meyer DM, Lauroesch JT, Peek JEG, Heiles C. 2012. *Ap. J.* 752(2):119
Miville-Deschênes MA, Joncas G, Falgarone E, Boulanger F. 2003. *Astron. Astrophys.* 411:109–21
Moss VA, McClure-Griffiths NM, Murphy T, et al. 2013. *Ap. J. Suppl.* 209(1):12
Muller CA, Oort JH. 1951. *Nature* 168(4270):357–58
Murray CE, Lindner RR, Stanimirović S, et al. 2014. *Ap. J. Lett.* 781(2):L41
Murray CE, Peek JEG, Kim C-G. 2020. *Ap. J.* 899(1):15
Murray CE, Stanimirović S, Goss WM, et al. 2015. *Ap. J.* 804(2):89
Murray CE, Stanimirović S, Goss WM, et al. 2018. *Ap. J. Suppl.* 238(2):14
Murray CE, Stanimirović S, Heiles C, et al. 2021. *Ap. J. Suppl.* 256(2):37
Murray CE, Stanimirović S, Kim C-G, et al. 2017. *Ap. J.* 837(1):55
Nguyen H, Dawson JR, Lee MY, et al. 2019. *Ap. J.* 880(2):141
Nguyen H, Dawson JR, Miville-Deschênes MA, et al. 2018. *Ap. J.* 862(1):49
Nidever DL, Price-Whelan AM, Choi Y, et al. 2019. *Ap. J.* 887(2):115
Normandeau M, Taylor AR, Dewdney PE. 1996. *Nature* 380:687–89
Ntormousi E, Burkert A, Fierlinger K, Heitsch F. 2011. *Ap. J.* 731(1):13
Offner SSR, Arce HG. 2014. *Ap. J.* 784(1):61
Panopoulou GV, Lenz D. 2020. *Ap. J.* 902(2):120
Payne HE, Dickey JM, Salpeter EE, Terzian Y. 1978. *Ap. J. Lett.* 221:L95–98
Peek JEG, Babler BL, Zheng Y, et al. 2018. *Ap. J. Suppl.* 234(1):2

Peek JEG, Clark SE. 2019. *Ap. J. Lett.* 886(1):L13
Peek JEG, Heiles C, Peek KMG, Meyer DM, Lauroesch JT. 2011. *Ap. J.* 735(2):129
Peek JEG, Tchernyshyov K, Miville-Deschênes MA. 2022. *Ap. J.* 925(2):201
Pidopryhora Y, Lockman FJ, Dickey JM, Rupen MP. 2015. *Ap. J. Suppl.* 219(2):16
Pidopryhora Y, Lockman FJ, Shields JC. 2007. *Ap. J.* 656:928–42
Pingel NM, Lee MY, Burkhart B, Stanimirović S. 2018. *Ap. J.* 856(2):136
Pingel NM, Stanimirović S, Peek JEG, et al. 2013. *Ap. J.* 779(1):36
Piontek RA, Ostriker EC. 2004. *Ap. J.* 601(2):905–20
Piontek RA, Ostriker EC. 2005. *Ap. J.* 629(2):849–64
Piontek RA, Ostriker EC. 2007. *Ap. J.* 663(1):183–203
Pisano DJ. 2014. *Astron. J.* 147(3):48
Price-Whelan AM, Nidever DL, Choi Y, et al. 2019. *Ap. J.* 887(1):19
Pritchard JR, Loeb A. 2012. *Rep. Prog. Phys.* 75:086901
Putman ME, Peek JEG, Joung MR. 2012. *Annu. Rev. Astron. Astrophys.* 50:491–529
Radhakrishnan V, Goss WM. 1972. *Ap. J. Suppl.* 24:161–66
Rathjen TE, Naab T, Girichidis P, et al. 2021. *MNRAS* 504(1):1039–61
Reid MJ, Menten KM, Brunthaler A, Zheng XW, Dame TM, et al. 2019. *Ap. J.* 885(2):131
Roy N, Kanekar N, Braun R, Chengalur JN. 2013a. *MNRAS* 436(3):2352–65
Roy N, Kanekar N, Chengalur JN. 2013b. *MNRAS* 436(3):2366–85
Rybarczyk DR, Stanimirović S, Gong M, et al. 2022. *Ap. J.* 928(1):79
Saintonge A, Catinella B. *Annu. Rev. Astron. Astrophys.* 60:319–61
Sault RJ. 1994. *Astron. Astrophys. Suppl. Ser.* 107:55–69
Savage BD, Wakker BP. 2009. *Ap. J.* 702(2):1472–89
Scalo J, Elmegreen BG. 2004. *Annu. Rev. Astron. Astrophys.* 42:275–316
Scalo JM. 1987. In *Interstellar Processes*, ed. DJ Hollenbach, HA Thronson, pp. 349–92. Berlin: Springer
Schruba A, Leroy AK, Walter F, et al. 2011. *Astron. J.* 142(2):37
Seifried D, Beuther H, Walch S, et al. 2022. *MNRAS* 512(4):4765–84
Seon K-i, Kim C-G. 2020. *Ap. J. Suppl.* 250(1):9
Shaver PA, McGee RX, Newton LM, Danks AC, Pottasch SR. 1983. *MNRAS* 204:53–112
Shull JM, Danforth CW, Anderson KL. 2021. *Ap. J.* 911(1):55
Sidorin V, Douglas KA, Palouš J, Wünsch R, Ehlerová S. 2014. *Astron. Astrophys.* 565:A6
Snow TP, McCall BJ. 2006. *Annu. Rev. Astron. Astrophys.* 44:367–414
Sofue Y. 2018. *Publ. Astron. Soc. Jpn.* 70(3):50
Soler JD, Beuther H, Rugel M, et al. 2019. *Astron. Astrophys.* 622:A166
Soler JD, Beuther H, Syed J, et al. 2020. *Astron. Astrophys.* 642:A163
Soler JD, Miville-Deschênes MA, Molinari S, et al. 2022. *Astron. Astrophys.* 662:A96
Spitzer L Jr. 1978. *Physical Processes in the Interstellar Medium*. New York: Wiley
Stanimirović S. 2002. *Publ. Astron. Soc. Pac.* 278:375–96
Stanimirović S, Murray CE, Lee MY, Heiles C, Miller J. 2014. *Ap. J.* 793(2):132
Stanimirović S, Putman M, Heiles C, et al. 2006. *Ap. J.* 653:1210–25
Stanimirović S, Staveley-Smith L, Dickey JM, Sault RJ, Snowden SL. 1999. *MNRAS* 302:417–36
Stanimirović S, Zweibel EG. 2018. *Annu. Rev. Astron. Astrophys.* 56:489–540
Staveley-Smith L, Sault RJ, Hatzidimitriou D, Kesteven MJ, McConnell D. 1997. *MNRAS* 289:225–52
Stevens ARH, Diemer B, Lagos CDP, et al. 2019. *MNRAS* 483(4):5334–54
Stil JM, Lockman FJ, Taylor AR, et al. 2006. *Ap. J.* 637:366–79
Stil JM, Taylor AR, Dickey JM, et al. 2006. *Astron. J.* 132:1158–76
Strasser ST, Dickey JM, Taylor AR, et al. 2007. *Astron. J.* 134:2252–71
Syed J, Wang Y, Beuther H, et al. 2020. *Astron. Astrophys.* 642:A68
Szotkowski S, Yoder D, Stanimirović S, et al. 2019. *Ap. J.* 887(2):111
Taylor AR, Gibson SJ, Peracaula M, et al. 2003. *Astron. J.* 125:3145–64
Tchernyshyov K, Peek JEG. 2017. *Astron. J.* 153(1):8
Tchernyshyov K, Peek JEG, Zasowski G. 2018. *Astron. J.* 156(6):248

Turić L, Jelić V, Jaspers R, et al. 2021. *Astron. Astrophys.* 654:A5
Valdivia V, Hennebelle P, Gérin M, Lesaffre P. 2016. *Astron. Astrophys.* 587:A76
Van Eck CL, Haverkorn M, Alves MIR, et al. 2019. *Astron. Astrophys.* 623:A71
Vázquez-Semadeni E, Colín P, Gómez GC, Ballesteros-Paredes J, Watson AW. 2010. *Ap. J.* 715(2):1302–17
Vergely JL, Lallement R, Cox NLJ. 2022. arXiv:2205.09087 [astro-ph.GA]
Verschuur GL. 1995. *Ap. J.* 451:645–59
Wada K, Meurer G, Norman CA. 2002. *Ap. J.* 577(1):197–205
Walch S, Girichidis P, Naab T, et al. 2015. *MNRAS* 454(1):238–68
Wang Y, Beuther H, Rugel MR, et al. 2020a. *Astron. Astrophys.* 634:A83
Wang Y, Bihr S, Beuther H, et al. 2020b. *Astron. Astrophys.* 634:A139
Wenger TV, Balser DS, Anderson LD, Bania TM. 2019. *Ap. J.* 887(2):114
Winkel B, Kalberla PMW, Kerp J, Flöer L. 2010. *Ap. J. Suppl.* 188:488–99
Wolfire MG. 2015. *Highlights Astron.* 16:600–2
Wolfire MG, Hollenbach D, McKee CF, Tielens AGGM, Bakes ELO. 1995. *Ap. J.* 443:152–68
Wolfire MG, McKee CF, Hollenbach D, Tielens AGGM. 1995. *Ap. J.* 453:673–84
Wolfire MG, McKee CF, Hollenbach D, Tielens AGGM. 2003. *Ap. J.* 587:278–311
Wouthuysen SA. 1952. *Astron. J.* 57:31–32
Yoo H, Cho J. 2014. *Ap. J.* 780(1):99
Yuen KH, Ho KW, Lazarian A. 2021. *Ap. J.* 910(2):161
Yuen KH, Lazarian A. 2017. *Ap. J. Lett.* 837(2):L24